Physics – Uspekhi **66** (7) 704 – 721 (2023)

INSTRUMENTS AND METHODS OF INVESTIGATION PACS numbers: 52.40.Hf, 52.80.Vp, **79.70.+q**

Explosive emission processes in thermonuclear facilities with magnetic plasma confinement and in linear electron–positron colliders

S A Barengolts, G A Mesyats

DOI: https://doi.org/10.3367/UFNe.2022.02.039163

Contents

1. Introduction **704**

2. Phenomenological model of explosive electron emission **705**

2.1 Criterion for the initiation of a pulsed vacuum breakdown; 2.2 Parameters of explosive emission processes; 2.3 Simulation of microexplosive cathode processes; 2.4 Current action integral for microexplosive processes

3. Unipolar arcs in thermonuclear facilities with magnetic plasma confinement **708**

3.1 Factors contributing to the initiation of a unipolar arc; 3.2 Results of experimental studies of arc discharges with W-fuzz samples; 3.3 Explosive emission model for simulation of a radiofrequency vacuum breakdown; 3.4 Erosion characteristics of arc discharges with W-fuzz samples

4. Initiation of a vacuum breakdown in the accelerating structures of electron–positron colliders **715**

4.1 Criteria for the initiation of a radiofrequency vacuum breakdown; 4.2 Microexplosive processes in a radiofrequency vacuum breakdown; 4.3 Explosive emission model of a radiofrequency vacuum breakdown; 4.4 Simulation of prebreakdown processes

5. Conclusion **720**

References **720**

Abstract. A model of the phenomenon of explosive electron emission based on its similarity to the electrical explosion of conductors is presented. With this model, the microexplosive processes occurring on a cathode surface due to the action of the explosive emission current have been simulated. The simulation results have been used to analyze explosive emission processes caused by the operation of unipolar arcs in thermonuclear reactors with magnetic plasma confinement and by the initiation of radiofrequency vacuum breakdowns in the accelerating structures of linear electron–positron colliders. The structure of the arc discharge cathode spot and the erosion characteristics have been investigated for nanostructured tungsten (W-fuzz) surfaces formed in thermonuclear reactors with magnetic plasma confinement. For radiofrequency vacuum breakdowns, the initiating parameters have been estimated, and prebreakdown and microexplosive processes have been simulated.

S A Barengolts [1, 2, 3, a], **G A Mesyats** [2, b]
[1] Prokhorov General Physics Institute, Russian Academy of Sciences, ul. Vavilova 38, 119991 Moscow, Russian Federation
[2] Lebedev Physical Institute, Russian Academy of Sciences, Leninskii prosp. 53, 119991 Moscow, Russian Federation
[3] Institute of Electrophysics, Ural Branch of the Russian Academy of Sciences, ul. Amundsena 106, 620016 Ekaterinburg, Russian Federation
E-mail: [a] sabarengolts@mail.ru, [b] mesyats@sci.lebedev.ru

Received 25 January 2022
Uspekhi Fizicheskikh Nauk **193** (7) 751 – 769 (2023)
Translated by S A Barengolts

Keywords: pulsed vacuum breakdown, explosive electron emission, unipolar arc, cathode spot, field emission, radiofrequency vacuum breakdown

1. Introduction

The *International Thermonuclear Experimental Reactor* (ITER) project and the Compact Linear Collider (CLIC) project aimed at creating a *linear electron–positron collider* are the largest international scientific projects currently under implementation or under final development. These projects have seemingly completely different goals and objectives, suggesting different ways to achieve them. However, they involve a common problem, namely, the initiation of electrical discharge processes on surfaces exposed to high-temperature plasmas (ITER) or on the surfaces of accelerating structures exposed to radiofrequency electromagnetic waves (CLIC). In the first case, this is unipolar arcing, which is a source of various kinds of impurities, such as liquid metal drops, microparticles, low-temperature atoms and ions, and the like, that contaminate the thermonuclear plasma. In the second case, the initiation of vacuum breakdown gives rise to significant emission currents from the surface of the accelerating structure, reaching tens or even hundreds of amperes. The magnetic fields induced by these currents and the absorption of electromagnetic wave energy in the accelerating structure during the breakdown may sharply reduce the collider luminosity.

G A Mesyats supposed that the operation of a unipolar arc and the initiation of radiofrequency vacuum breakdown occur by the mechanism of explosive electron emission [1, 2].

The phenomenon of explosive electron emission was discovered in studying vacuum breakdowns caused by high voltage pulses of nanosecond duration [3]. It was found that the failure of vacuum insulation under these conditions is due to the appearance of plasma microbunches on the cathode (cathode flares). The propagation of cathode flares into the electrode gap is accompanied by a sharp increase in the emission current from the cathode. Studies of the phenomenon of explosive electron emission have shown that the transition of the cathode material to a plasma state occurs due to high energy concentrated in microvolumes on the cathode surface [4–6]. The main reason for the energy concentration is the resistive heating of cathode microprotrusions by the high-density field emission current. The plasma produced due to microexplosions occurring on the cathode propagates with high velocity (~ 10 km s^{-1}) into the electrode gap. This creates conditions for the compensation of the electron emission from the flare boundary immediately at the place where the flare is in contact with the cathode surface. The cathode area carrying the current of a vacuum discharge is called the cathode spot. A cathode spot includes a heated region of the cathode surface and the dense near-cathode plasma that is in contact with this region. The cathode material within a cathode spot, on a scale of several micrometers, goes from the solid to a plasma state. As time passes, cathode spots cover a larger and larger area of the cathode surface, and the vacuum discharge changes into a spark, which is characterized by a sharp increase in the explosive electron emission current. In this case, the magnitude of the explosive emission current is limited only by the parameters of the external circuit, which makes it possible to obtain practically unlimited (up to megaamperes) pulsed electron currents in the diode. This property of explosive electron emission was used to create unique instruments and devices for pulsed power technology [7].

Further investigations have shown that explosive electron emission is a fundamental phenomenon, and it reflects the reaction of the cathode surface to the action of intense energy flows and high electric fields [8]. This paper is devoted to another aspect of this phenomenon, which is also of great practical importance: cases in which explosive electron emission is an undesirable phenomenon and there is a need to find ways to suppress it. In particular, this refers to explosive emission processes that are initiated and self-sustained in metal–plasma contacts and on electrodes exposed to radiofrequency electromagnetic fields.

The fact that explosive emission processes play a decisive part in the discharge phenomena occurring in thermonuclear reactors with magnetic plasma confinement and in the accelerating structures of linear electron–positron colliders is evidenced primarily by the presence of microcraters, which are identical to those arising upon initiation of a pulsed vacuum breakdown, on surfaces that are in contact with the reactor plasma and exposed to electromagnetic waves. The main goal of this paper is to demonstrate that the use of simple estimates of the characteristics of explosive emission processes makes it possible to obtain a fairly clear idea of the mentioned phenomena. The paper is arranged as follows. Section 2 briefly outlines the main points of the explosive electron emission model based on the analogy with an electrical explosion of conductors and presents the results of a simulation of the microexplosive processes occurring on the cathode performed with the use of wide-range equations of state of matter. Section 3 presents the results of studying the explosive emission processes that occur in unipolar arcing under the conditions of thermonuclear reactors with magnetic plasma confinement, when a layer of nanofibers (W-fuzz) is formed on a tungsten surface exposed to helium plasma. Section 4 is devoted to the part played by explosive emission processes in the initiation of radiofrequency vacuum breakdowns on the surfaces of CLIC accelerating structures. Finally, in Section 5, the main conclusions based on the results of the study are presented.

2. Phenomenological model of explosive electron emission

2.1 Criterion for the initiation of a pulsed vacuum breakdown

As noted above, the phenomenon of explosive electron emission was discovered in studying the nanosecond vacuum breakdown between plane electrodes [3]. Since for plane cathodes there is always the problem of correctly determining the factor of field enhancement at the cathode microprotrusions, the emission area, etc., validation experiments were carried out with classical pointed field emitters, for which these parameters can well be controlled [9]. For each emitter, Fowler–Nordheim characteristics were preliminarily measured. The voltage pulse duration was varied from 0.7 ns to 4 μs. The breakdown initiation delay time t_d was determined as the time at which the emission current in the electrode gap began to sharply increase. As a result of these investigations, it was found that this time t_d and the current density j at the cathode are related as

$$j^2 t_d = \text{const}\,. \tag{1}$$

The solution to the nonstationary problem of the heating of a pointed cathode by the thermionic field emission current showed that the heat release in the cathode in the interval of a few to tens of nanoseconds occurs mainly by the mechanism of resistive heating [4]. The emissive source of energy release (Nottingham effect) affects the heating dynamics to some extent, but not decisively. As a result of the numerical simulation, relation (1) became

$$j^2 t_d = f\frac{\rho c}{\kappa_0}\,, \tag{2}$$

where ρ is the density of the cathode material, c is the specific heat capacity, and κ_0 is the temperature coefficient of electrical resistivity $\kappa = \kappa_0 T$. For a conical microprotrusion with a small cone angle, the factor f weakly depends on its geometry and is determined mainly by the choice of the temperature at which breakdown is initiated. This temperature was taken as the melting point, boiling point, or critical temperature [4, 5, 10, 11].

The existence of a relationship between current density and breakdown delay time, determined by relation (2), which depends only on the parameters of a particular material, made it possible to conclude that the processes involved in the initiation of vacuum breakdown are in many respects similar to those observed during electrical explosions of conductors [6, 8]. In both cases, the main mechanism of heat release is resistive heating of a metal by a high-density current, resulting in an explosive transition of the metal to a plasma state. The most important characteristic of an

electrical explosion of conductors is the integral of specific current action [12]

$$\bar{h} = \int_0^{t_d} j^2 \, dt , \tag{3}$$

which determines the delay time to the explosion of the conductor, and since the explosion occurs in the supercritical region when energy is rapidly deposited into the conductor (see, e.g., [13]), it determines in fact the time in which the material changes to a plasma state. With this in mind, the criterion for initiation of a pulsed vacuum breakdown (1) can be written as [8]

$$j^2 t_d \approx \bar{h} , \tag{4}$$

which includes the value of the current action integral obtained for (well controlled) conditions of the electrical explosion of the conductor.

2.2 Parameters of explosive emission processes

The use of the analogy between a vacuum breakdown and an explosion of conductors made it possible not only to obtain information about the processes leading directly to vacuum breakdown but also to estimate the most important parameters that determine the operation of the cathode spot of a vacuum discharge. In particular, the time dependence of the coordinate r_{ex} (or the cross section of a conical microprotrusion, $S = \Omega r_{ex}^2$) corresponding to the volume of the microprotrusion material changed to a plasma state can be expressed as

$$r_{ex} = \left(\frac{i^2 t}{\Omega^2 \bar{h}} \right)^{1/4} , \tag{5}$$

where $\Omega = 2\pi (1 - \cos\theta)$, θ is the cone angle, and i is the current carried by the microprotrusion.

Obviously, the destruction of a cathode microprotrusion cannot last indefinitely. It is logical to suppose that the destruction stops when its rate becomes lower than the rate of heat removal to the bulk cathode, i.e., at a time when $dr_{ex}/dt \approx d(at)^{1/2}/dt$, where a is the thermal diffusivity of the material. Hence, the lifetime of the emission center can be estimated as

$$\tau_e = \frac{i^2}{16\Omega^2 a^2 \bar{h}} \tag{6}$$

and the coordinate r_{cr} that determines the volume of the conical microprotrusion material having changed to a plasma state as

$$r_{cr} = \frac{i}{2\Omega\sqrt{a\bar{h}}} . \tag{7}$$

Knowing the volume of the microprotrusion material that changed to a plasma state, we can easily estimate one of the key characteristics of the vacuum discharge, which determines the process of generation of a conducting medium in the electrode gap. This is the process by which a vacuum discharge operates. The quantitative characteristic of this process is the rate of ion erosion, γ_i, which is defined as the ratio of the mass of the cathode material removed in the form of ions to the charge passed through the microprotrusion q:

$$\gamma_i = \frac{2}{3} \rho \sqrt{\frac{a}{\bar{h}}} . \tag{8}$$

As can be seen from expression (8), the ion erosion rate does not depend on the current or microprotrusion geometry. It is determined only by the characteristics of the cathode material, namely, by its density, thermal diffusivity, and specific current action integral.

The processes occurring in the cathode spot of a vacuum discharge are cyclical due to the finite lifetime of the emission center. This fact, as well as estimates made by using the analogy between an explosion of conductors and a vacuum discharge, was used in the development of the ecton model of the cathode spot of a vacuum arc [8, 14–16]. According to this model, the cathode spot consists of individual cells. The cells are explosive emission centers, each emitting a portion of electrons, called an ecton. A cycle consists of two stages: the ecton operation stage and a short stage during which a new explosive emission center is initiated to replace the one that has died. The conditions for the initiation of a new ecton process, namely, the presence of a dense near-cathode plasma and liquid-metal microirregularities of the surface, arise during the previous ecton process [8, 14–19]. The current carried by a spot cell, i_c, is approximately two threshold currents of the arc operation, as was established by Kesaev in studying the structure of the cathode spot of a vacuum arc [20]. Using the ecton model of a cathode spot, an explanation was given for the main effects and characteristics of a vacuum arc discharge, such as the threshold current, cathode fall voltage, spontaneous extinction of the discharge, and the Tanberg effect [8]. It was shown that the parameters of the arc plasma take their finite values during the operation of a spot cell [21, 22]. An increase in the arc current up to a kiloampere is accompanied by a mere increase in the number of simultaneously operating ectons, which explains the experimental data showing a weak dependence of the ion flow parameters on the vacuum arc current.

2.3 Simulation of microexplosive cathode processes

Direct use of the results of investigations on the explosion of conductors for analyzing microexplosive processes involved in a vacuum discharge requires a more rigorous justification due to the obvious differences between these phenomena. A cathode microprotrusion is a conductor segment about a micrometer in length having a free (vacuum) boundary on one side and a bulk cathode on the other. An ordinary conductor can be considered to be heated uniformly along its length (if instabilities are disregarded), whereas, when a cathode microprotrusion explodes, additional heat is transferred to the bulk cathode, leading not only to the removal of energy but also to the fact that the explosive destruction of the microprotrusion begins from its top. Therefore, an additional component of the gas-kinetic pressure arises, the gradient of which, normal to the microprotrusion cross section, is directed from top to base.

The microexplosive processes occurring on a cathode were simulated using the JULIA code [23], based on a particle-in-cell method, which was previously used to simulate the explosion of conductors in a two-dimensional approximation (see, e.g., [24]). This code, adapted to calculate the heating of cathode microprotrusions, included a system of hydrodynamic equations describing the laws of

conservation of mass, momentum, and energy,

$$\frac{\partial \rho}{\partial t} + \nabla(\rho \mathbf{v}) = 0\,, \tag{9}$$

$$\rho \frac{\partial \mathbf{v}}{\partial t} + \rho \mathbf{v} \nabla \mathbf{v} = -\nabla p + \frac{1}{c}\,\mathbf{j} \times \mathbf{H}\,, \tag{10}$$

$$\frac{\partial \rho \varepsilon}{\partial t} + \nabla(\rho \varepsilon \mathbf{v}) = -p \nabla \mathbf{v} + \frac{\mathbf{j}^2}{\sigma} + \nabla(\lambda \nabla T)\,, \tag{11}$$

Maxwell's equations, written in a quasi-stationary approximation (not taking into account displacement currents),

$$\frac{1}{c}\frac{\partial \mathbf{H}}{\partial t} = -\nabla \times \mathbf{E}\,, \quad \nabla \times \mathbf{H} = \frac{4\pi}{c}\,\mathbf{j}\,, \tag{12}$$

and Ohm's law

$$\mathbf{j} = \sigma\left(\mathbf{E} - \frac{1}{c}\,\mathbf{v} \times \mathbf{H}\right), \tag{13}$$

where p, ε, and T are, respectively, the pressure, internal energy, and temperature of the material; $\mathbf{v}$ is its velocity; $\mathbf{H}$ is the magnetic field strength; $\mathbf{E}$ is the electric field strength; $\mathbf{j}$ is the current density; and λ and σ are, respectively, the thermal and the electrical conductivity of the material.

The problem was solved in the following statement. It was assumed that the explosive electron emission had already been initiated, so the current through the microprotrusion was determined by the parameters of the external circuit. The cathode–microprotrusion system was included in the electrical circuit, which was described by the equation

$$U_{\text{out}} = I(t) R_{\text{out}} + U_{\text{load}}(t)\,, \tag{14}$$

where $U_{\text{out}}(t)$ is the external source voltage, which increased to $U_0 = 3200$ V in 0.1 ns and then remained constant; $R_{\text{out}} = 1000\ \Omega$ is the external resistance, the value of which was chosen so that the short-circuit current in the circuit would be equal to 3.2 A; and $U_{\text{load}}(t)$ is the voltage drop across the load (cathode–microprotrusion system). The value of the current $I(t)$ was used as a boundary condition in solving the Maxwell's equations (12). It was assumed that a microprotrusion shaped like a cylinder 1.5 μm high is located on the surface of a plane copper cathode. In the calculations, the radius of the cylinder, r_c, was varied between 0.2 and 0.4 μm.

Copper (CLICK accelerating structure) and tungsten (ITER divertor) were chosen as test materials. The current was set equal to 3.2 A, which corresponds to the (doubled threshold) current carried by an individual cell (ecton) of the vacuum arc cathode spot for copper and tungsten cathodes [8, 20]. The geometric dimensions of the microprotrusion corresponded to those observed during the initiation of a vacuum breakdown and explosive electron emission [6, 25].

The method used for solving the system of equations (9)–(14) is described in detail in [26, 27]. The calculations were performed using wide-range semi-empirical equations of state and tabular data on the conductivity of copper and tungsten [28, 29].

It should be noted that a similar approach to simulating the explosion of microprotrusions invoking wide-range equations of state was used previously [30–33]. However, the purpose of these papers was to study the products of the explosion of a microprotrusion [30, 31] or the initial stage of crater formation and the parameters of the produced plasma [32, 33]. The parameters of microexplosive processes and, in particular, the current action integral were not investigated in detail. At the same time, the system of equations (9)–(14) was solved using modern methods (in particular, a particle-in-cell method) to simulate the parameters of the explosion-produced plasma and more accurate equations of state to describe the states of the cathode material, including metastable ones [26, 27]. The use of these equations made it possible to rigorously trace the state of the material during the explosion of a microprotrusion and obtain detailed information on the interaction of the explosion-produced plasma with the liquid metal formed in the operating zone of the cathode spot of a vacuum discharge [19].

2.4 Current action integral for microexplosive processes

Figure 1 shows the time dependence of the voltage across the load during the explosion for a thin wire and a cathode microprotrusion. Using these plots, one can estimate the value of the current action integral, which is usually determined for the time interval between the beginning of the voltage pulse and the point at which the voltage peaks, t_{ex}. At a current density of 1.1×10^9 A cm^{-2}, the integral equals 2.43×10^9 A^2 s cm^{-4} ($t_{\text{ex}} = 1.9$ ns) for the exploded thin wire and 3.1×10^9 A^2 s cm^{-4} ($t_{\text{ex}} = 2.6$ ns) for the cathode microprotrusion ($r_c = 0.3$ μm). It decreases to 2.7×10^9 A^2 s cm^{-4} as the current density is decreased to 6.4×10^8 A cm^{-2} ($r_c = 0.4$ μm).

The difference in the values of the current action integral might occur due to different methods of its determination. Figure 2 shows the temperature distribution and the phase state for a copper cathode microprotrusion at a time of 2.2 ns. As can be seen from this figure, the top of the microprotrusion has been heated to a temperature of 1.4 eV and is in a plasma state, while the temperature of the rest of the microprotrusion decreases monotonicly to about 0.2 eV at the base. As can be seen from Fig. 2b, the microprotrusion, with the exception of its top, is in a liquid state with small two-phase (liquid plus gas) inclusions. The current action integral determined by the time at which the top material has changed to a plasma state is 2.6×10^9 A^2 s cm^{-4}. Anyway, in view of the different conditions for the explosion between thin wires and cathode microprotrusions, the difference between the current action integral values is not significant. Therefore, in what follows, we will use its value obtained by the traditional method for a microprotrusion entirely subjected to explosive destruction.

Similar results were obtained in studying the current action integral for tungsten microprotrusions. Figure 3 shows the time dependence of the load voltage at a current density of 1.1×10^9 A cm^{-2}. The value of the current action integral, determined for the time the voltage peaked, is 2×10^9 A^2 s cm^{-4}. When the current density was decreased to 6.4×10^8 A cm^{-2}, the current action integral decreased to 1.6×10^9 A^2 s cm^{-4} [34], whereas for the explosion of a tungsten wire it is 1.85×10^9 A^2 s cm^{-4} [13]. It should be noted that the tendency for the current action integral to decrease with decreasing current density is also characteristic of the explosion of thin wires. The reason for this decrease is that, when energy is rapidly deposited into a conductor (microprotrusion), inertial forces keep its material in a liquid state, thereby increasing the energy input in the conductor before the explosion [13, 35].

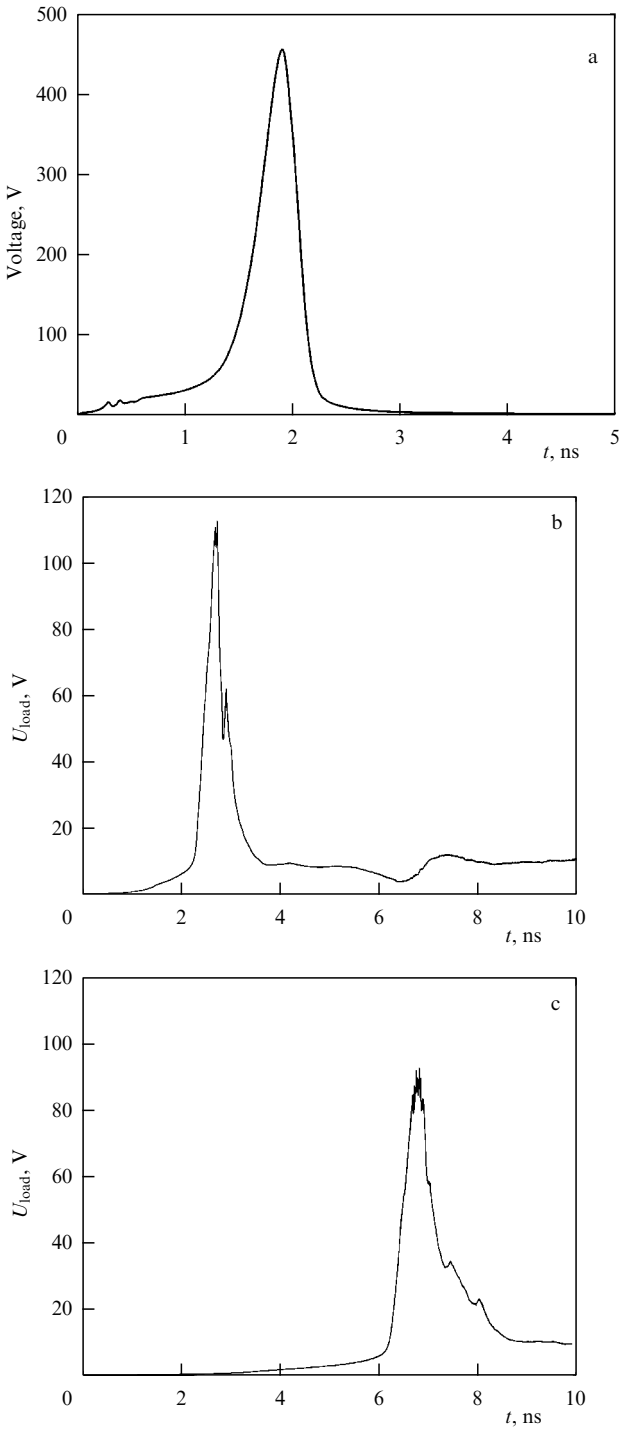

Figure 1. Time dependence of voltage across a load: a thin copper wire of radius 0.3 μm (a) and a copper cathode microprotrusion of radius 0.3 (b) and 0.4 μm (c). Current is 3.2 A for all cases.

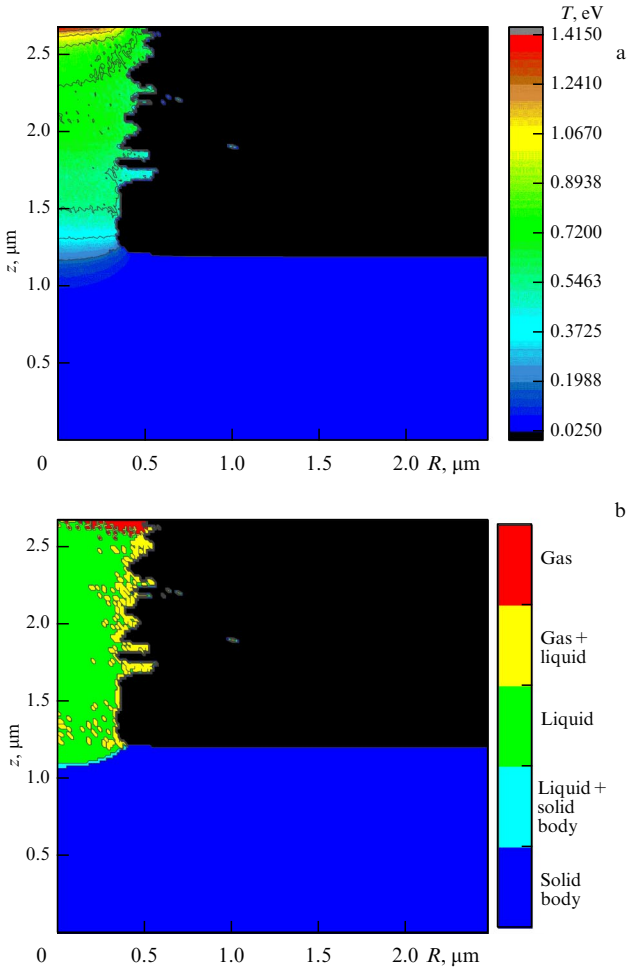

Figure 2. Temperature distribution (a) and phase state (b) at a time of 2.2 ns for a copper cathode microprotrusion. Current is 3.2 A; $r_c = 0.3$ μm.

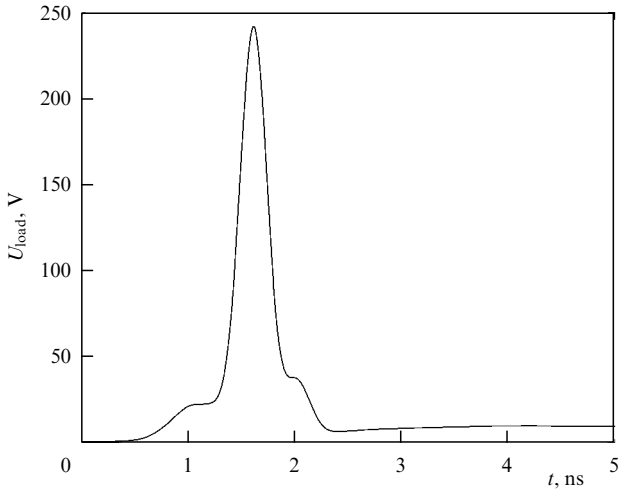

Figure 3. Time dependence of the load voltage for a tungsten cathode microprotrusion during its heating. Current is 3.2 A; $r_c = 0.3$ μm.

The above results on the calculation of the explosion of a microprotrusion allow the conclusion that its analogy to the electrical explosion of conductors, invoked previously to estimate the parameters of the initiation of a breakdown and of the processes occurring in the cathode spot of a vacuum discharge, is quite justified. We will use below the values of the current action integral obtained for tungsten and copper cathode microprotrusions to analyze the mechanisms involved in the operation of unipolar arcs and in the initiation of radiofrequency vacuum breakdown.

3. Unipolar arcs in thermonuclear facilities with magnetic plasma confinement

3.1 Factors contributing to the initiation of a unipolar arc

Unipolar arcs are arc discharges that occur when a metal surface is exposed to a plasma [36]. Arc discharges of this type

are sustained by the potential difference between the wall and the plasma that arise due to the thermal motion of the plasma electrons. A discharge of this type is called a unipolar arc since it is sustained with no external source and its current circulates between the plate and the plasma.

Unipolar arcing manifests itself primarily through the microcraters that are formed at places of contact between the plasma and the electrode. Unipolar arcs were intensely studied in the 1970s–1980s, when they were detected in almost all thermonuclear facilities [37]. It was believed that unipolar arcs were the main suppliers of impurities that polluted the reactor plasma. Along with the study of unipolar arcs in tokamaks, a number of experiments were carried out on their initiation on metal surfaces exposed to intense radiation and plasma flows [38–42]. In these experiments, it was convincingly proved that the formation of craters on the exposed surface is associated with the eroding effect of the arc plasma rather than with the action of an external energy source. However, the experimental material accumulated in studying unipolar arcs has not led to significant progress in understanding this phenomenon: "there are no reliable experimental data on the discharge conditions leading to arcing or on the frequency of arc occurrence" [43]. This was due to objective difficulties in studying this phenomenon associated with spontaneous and short-term arcing, the uncontrollability of the arcing parameters, and the creation of special conditions for arc initiation such as 'dirty' electrodes and external effects. Moreover, the model of a 'hot spot' as a source of erosive plasma with an emission current density of 10^8 A cm^{-2} [44] was generally accepted, but the mechanism of its operation remained obscure.

Interest in studying this phenomenon also decreased due to the use of a divertor in thermonuclear facilities, so that the plasma was confined by the magnetic separatrix rather than by the wall, a significant improvement in the conditions for confining thermonuclear plasma, and the proposed use of carbon as the material of the first wall. However, subsequent investigations of the properties of carbon in thermonuclear facilities showed that it was highly dispersed under the action of the reactor plasma, and the carbon layers deposited on the walls could accumulate and keep a large amount of tritium for a long time [45]. Therefore, tungsten was chosen as the material for the ITER divertor: it not only captures and keeps a small number of hydrogen isotopes, but also is able to withstand high thermal loads due to its high melting point and thermal conductivity, and, additionally, it has a high sputtering energy threshold.

Despite significant progress made in improving the conditions for thermonuclear plasma confinement, over the past 10 years, unipolar arcs have been detected in many thermonuclear facilities such as the ASDEX upgrade (Axially Symmetric Divertor Experiment Upgrade) [46–48], the LHD (Large Helical Device) [49], DIII-D [50–52], JT-60U [53], T-10 [54], and W7-X [55]. To initiate an arc discharge on pure tungsten, its surface should be exposed to a power density of about 100 MW cm^{-2} [56]. It is obvious that this power density is unattainable in the stationary operating conditions of future thermonuclear facilities, for which it is expected to be about 1 kW cm^{-2} [57]. However, two factors significantly increase the probability of unipolar arcing in thermonuclear facilities. The first is the repetitive magnetohydrodynamic instability of the thermonuclear plasma that shows up as Edge-Localized Modes (ELMs). In this case, the plasma acting on the divertor produces a power density of about 1 MW cm^{-2} [43, 58]. The second factor is the change in the surface morphology of tungsten exposed to helium plasma [59, 60]. Helium ions are generated in the course of thermonuclear reactions. A tungsten surface exposed to helium plasma becomes nanostructured ('fuzzed'). The conditions for the formation of fuzz arise when the temperature of the tungsten surface is in the range of 1000–2000 K and the energy of the incident helium ions is above 20 eV [61]. It is these divertor surface temperatures and incident ion energies that are inherent, according to estimates, in stationary plasma confinement modes [57, 62, 63]. A fuzz layer consists of individual fibers 10–20 nm thick which involve cavities containing helium atoms.

3.2 Results of experimental studies of arc discharges with W-fuzz samples

The experimental modeling of the effect of ELMs on fuzz structures carried out at the NAGDIS-II (Nagoya University Divertor Plasma Simulator II) facility made possible, perhaps for the first time, the direct, controlled, and long-term observation of unipolar arcing [64, 65]. Unipolar arcing was initiated by irradiating a tungsten plate $20 \times 20 \times 0.2$ mm in size, placed in a helium plasma of density $n_{pl} \approx 2 \times 10^{13}$ cm^{-3} and electron temperature $T_e \approx 6$ eV, with a 694-nm laser. Since that time, a series of studies of various characteristics of vacuum arc discharges with W-fuzz cathodes has been carried out. Most of the experiments were performed at the NAGDIS-II facility; similar experiments were also carried out at the PISCES-A (Plasma Interaction Surface Component Experimental Station A) (University of California, Los Angeles, USA) and MEVVA.Ru (Institute of High Current Electronics, Siberian Branch, Russian Academy of Sciences, Tomsk) facilities.

In short, the following main properties of arc discharges with W-fuzz samples were revealed:

(1) An arc with a current of a few amperes was stably initiated in a helium plasma when the tungsten plate potential was no greater than -55 V [66] and the threshold value of the potential decreased with an increase in current, [67]. The arc operation voltage increased almost linearly from 36 to 65 V as the arc current was increased from 4 to 26 A [68].

(2) The threshold arc operation current was found to be 1.5–2 A. The duration of arc operation at these currents is a few milliseconds [69].

(3) The velocity of motion of a cathode spot in a tangential magnetic field was found to depend on the thickness of the nanostructured layer. At a thickness of 1 μm, this velocity was 1.5×10^4 m s^{-1} and decreased to about an eighth of that value at a thickness of 5 μm. In this case, the width of the spot track increased by about a factor of five [70, 71].

(4) The erosion rate was also found to depend on the thickness of the nanostructured layer: it increased sharply from 0.5 to 1.5 mg C^{-1} as the thickness was increased to above 2 μm [68]. At this thickness, grouping of the cathode spot cells occurred, and this resulted in a sharp broadening of the track of the spot during its motion in an external magnetic field [72].

(5) The plasma electron temperature, according to spectroscopic measurements, was in the range of 0.5–1 eV [73–75]. The mean charge of tungsten ions in the arc plasma was $+1$, and it increased as the nanostructured layer was destroyed under the action of arc discharge pulses [76].

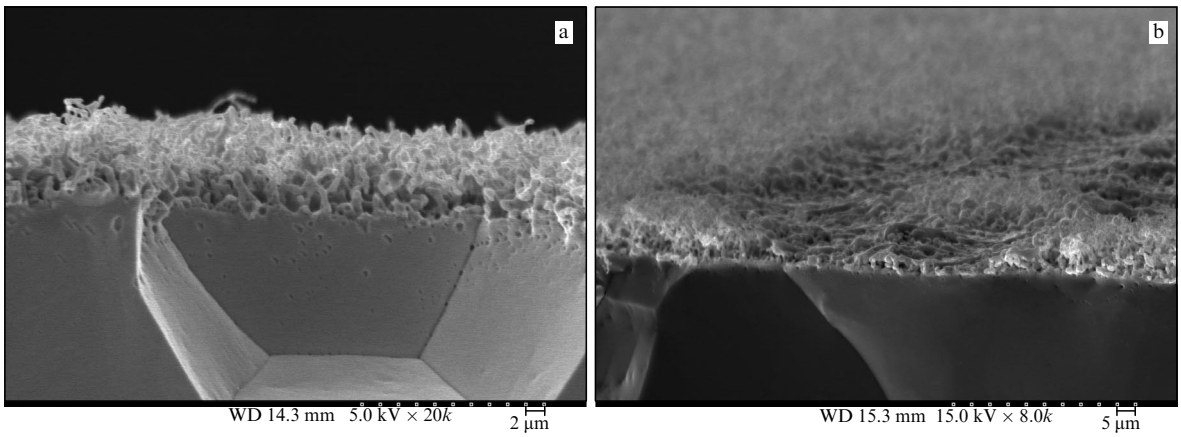

Figure 4. SEM images of a fuzz structure taken before (a) and after (b) the action of an arc discharge.

Before analyzing the processes occurring directly in the cathode spot and arc plasma of W-fuzz samples, we would like to make a few remarks regarding the technique of the experiments performed at the NAGDIS-II and PISCES-A facilities. All experiments were carried out with tungsten plates placed in helium plasma, mostly in an external tangential magnetic field, i.e., the cathode spots moved in the direction opposite to that of Ampère's force. The helium plasma was responsible for some features of the discharge operation, such as a relatively low plate potential at which the discharge was initiated and an increase in the discharge operation voltage with arc current (see Section 3.1). We have shown that these discharge properties, which are not typical of a conventional vacuum arc, were related to a decrease in potential in the helium plasma during the passage of the discharge current [67, 68].

Figure 4 shows SEM images of a fuzz structure formed on a tungsten surface and the track of the cathode spot after the action of an arc discharge. The presence of this structure, consisting, as mentioned above, of individual nanofibers 10–20 nm thick, leaves no doubt that the arc discharge operation was self-sustained through the explosive emission (ecton) mechanism. This was related to the high field enhancement factor β_E [77] and current density gain β_j [78]. The latter quantity determines the increase in current density over the nanofiber cross section through which the total current flows from the top and side surface above the cross section, regardless of the nature of this current (emission current or ion current from the plasma).

The fuzz layer formed on a tungsten plate not only significantly improves the conditions for the occurrence of explosive emission processes, but also radically changes the properties of the tungsten surface. In particular, the fuzz density was about 6% of the density of pure tungsten [79], and the thermal conductivity of the tungsten surface layer sharply decreased due to the small transverse dimensions of the nanofibers and helium atoms embedded in them [80]. As can be seen from the image of the spot track, a significant burnout of the nanostructured layer occurred during the operation of the arc discharge, but the spot did not pass to the smooth tungsten surface. Thus, it can be concluded that the conditions for the operation of an arc discharge in the presence of a fuzz structure are more favorable than those for a pure tungsten cathode, which manifests itself, in particular, in stable discharge operation at currents of a few amperes.

3.3 Explosive emission model for simulation of a radiofrequency vacuum breakdown

We proposed an explosive emission (ecton) model of the operation of a cathode spot on a nanostructured tungsten surface [81]. According to this model, the spot consists of individual cells (explosive emission centers), the operation time of which is determined by the burnout time of the nanostructured layer (Fig. 5).

The spot cells, upon their operation, leave micrometer-size craters on the surface, which are visible especially clearly for nanostructured layers of small thickness in any image of the spot track (Fig. 6). In this model, fuzz is considered a special medium, which is different from tungsten in arcing properties. For a spot operating on a flat surface, formulas (5)–(7) appear as follows:

The time-dependent radius of the crater formed upon the operation of a spot cell is described as

$$r_{\mathrm{exf}} = \sqrt{\frac{i_{\mathrm{c}}}{2\pi}}\left(\frac{t}{\bar{h}_{\mathrm{f}}}\right)^{1/4}, \tag{15}$$

the cell lifetime, as

$$\tau_{\mathrm{ef}} = \frac{i_{\mathrm{c}}^2}{64\pi^2 a_{\mathrm{f}}^2 \bar{h}_{\mathrm{f}}}, \tag{16}$$

and the crater radius, as

$$r_{\mathrm{crf}} = \frac{i_{\mathrm{c}}}{4\pi\sqrt{a_{\mathrm{f}}\bar{h}_{\mathrm{f}}}}, \tag{17}$$

where i_{c} is the current through the cell, and $\bar{h}_{\mathrm{f}}$ and a_{f} are, respectively, the current action integral and thermal diffusivity of the fuzz structure.

It should be noted that, according to (16), the operation time of a spot cell on a smooth tungsten surface at a current of a few amperes is not above some tenths of a nanosecond. That is why only the fuzz layer burns out and the spot does not pass to the clean surface of the tungsten plate when the layer thickness is small.

To estimate the parameters of a cell of the cathode spot of an arc on a tungsten cathode with a fuzz layer by using formulas (15)–(17), we need to know the current action integral and the cell current. The thermal diffusivity and thermal conductivity of tungsten fuzz were measured in [80]. Let us estimate the current action integral for W-fuzz cathodes. For the case of adiabatic heating of the cathode material by a high-density current flowing through the cathode, the specific

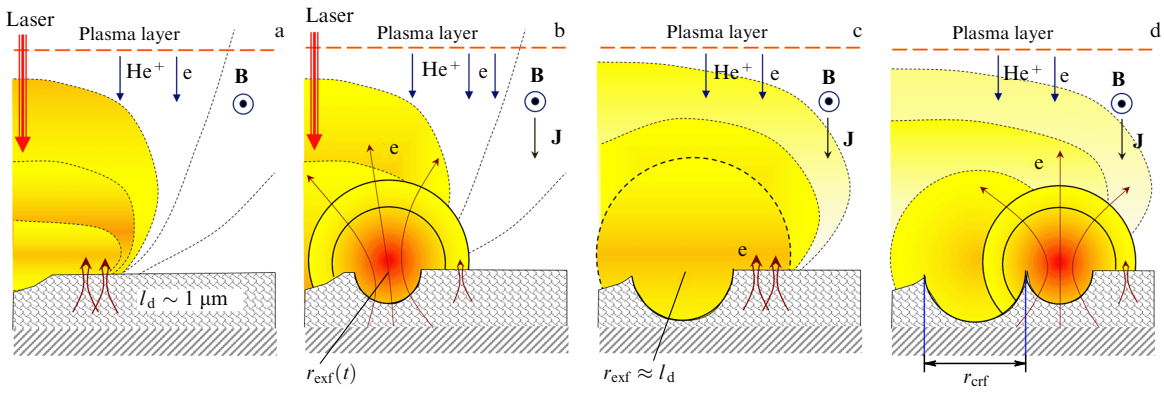

Figure 5. Sketch illustrating the ecton model of a laser-initiated unipolar arc discharge [82].

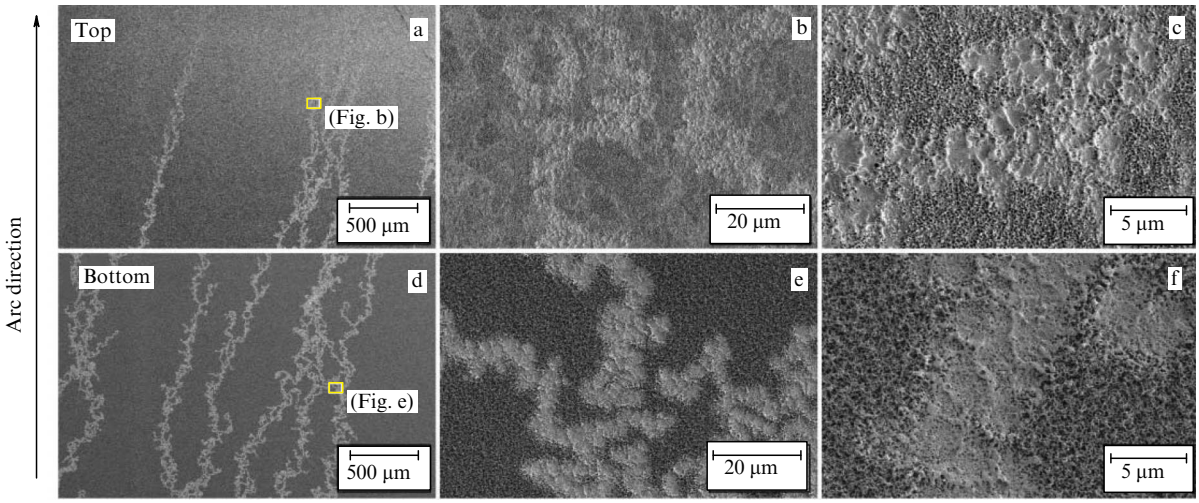

Figure 6. Track of a cathode spot moved over the surface of a tungsten cathode with a fuzz structure of thickness 1 μm. Arc current is 4 A [72].

current action integral can be written as [8]

$$\bar{h} = \int_{w_0}^{w_{cr}} \frac{\rho(w)}{\kappa(w)}\, \mathrm{d}w\,, \tag{18}$$

where w_{cr} is the energy density deposited to the cathode before its explosion. With the assumption of a linear dependence of resistivity on temperature, $\kappa = \kappa_0 T$, which is typical of most metals, (18) becomes

$$\bar{h} = \frac{\rho c}{\kappa_0} \ln \frac{T_{cr}}{T_0}\,, \tag{19}$$

where c is the heat capacity, T_{cr} is the critical temperature of the material, and T_0 is the initial temperature. Then, the ratio of the specific current action integrals can be expressed as

$$\frac{\bar{h}_f}{\bar{h}_W} = \frac{0.06\kappa_{0W}}{\kappa_{0f}}\,, \tag{20}$$

where $\bar{h}_W$ and κ_{0W} are, respectively, the specific current action integral and the temperature coefficient of resistance of pure tungsten. When writing (20), it was assumed that T_{cr} does not change upon the formation of W-fuzz; below, we will discuss the validity of this assumption. For the quantity $\bar{h}_W$, which varies with current density, we take an average value equal to 1.5×10^9 A^2 s cm^{-4} (see Section 1).

The change in the current action integral value after the formation of a fuzz structure is primarily associated with a decrease in the mean free path of electrons due to the small size of nanofibers and the presence of cavities containing helium atoms. This shows up as a sharp decrease in thermal conductivity and, accordingly, an increase in electrical resistance. The temperature coefficient of resistance, κ_{0f}, can be estimated from the Wiedemann–Franz–Lorentz law

$$\kappa_{0f} = \frac{L}{\lambda_f}\,, \tag{21}$$

where $L \approx 2.84 \times 10^{-8}$ V K^{-2} is the Lorentz constant for tungsten and $\lambda_f = 0.015$ W cm^{-1} is the thermal conductivity of W-fuzz [80]. As a result, we have $\bar{h}_f \approx 1.4 \times 10^6$ A^2 s cm^{-4} (we used $\kappa_{0w} \approx 3 \times 10^{-8}$ Ω cm for tungsten [82]).

Using the obtained value of the specific current action integral and expressions (15) and (17), we can estimate the radius of the crater formed on the W-fuzz surface as a function of time and spot cell current as

$$r_{exf} = 0.65\,(i_c^2 t)^{1/4} \tag{22}$$

and the radius of the crater formed due to Joule heating as

$$r_{crf} = 2.2 i_c\,. \tag{23}$$

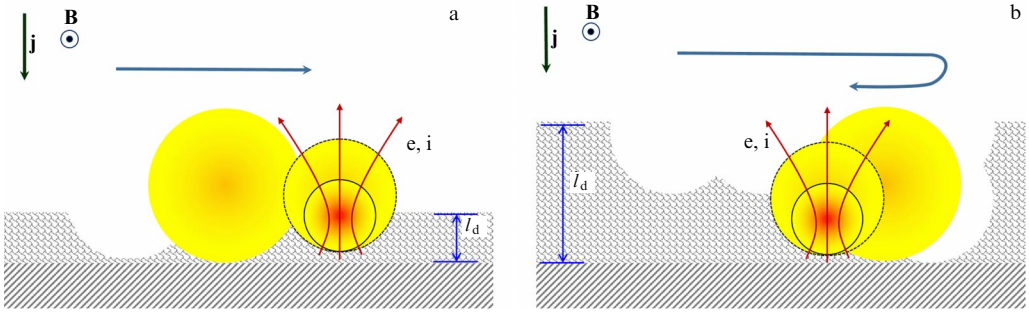

Figure 7. Sketch illustrating the motion of a cathode spot in an external magnetic field in the case of a fuzz layer l_d of small thickness (a) and large thickness (b).

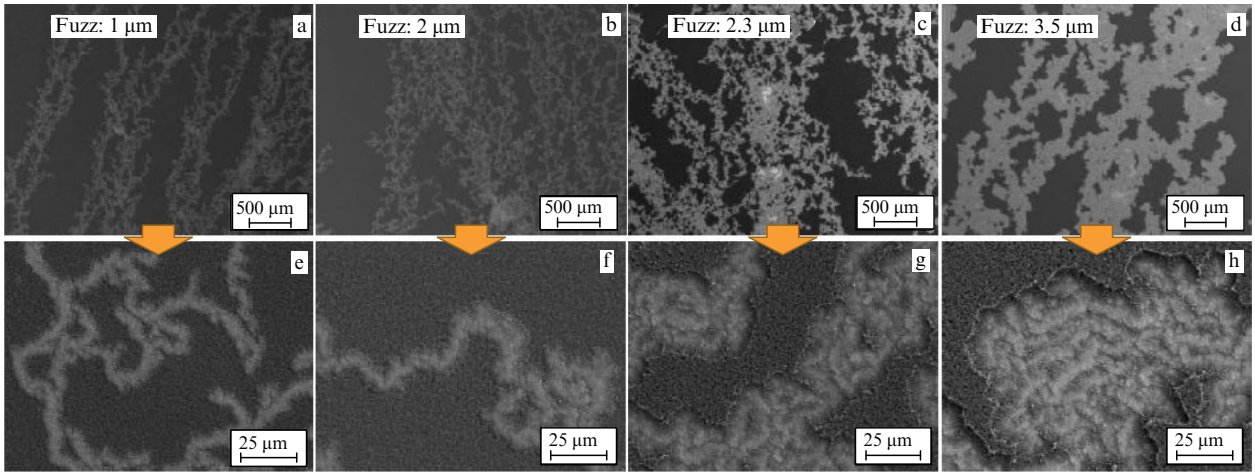

Figure 8. Erosion tracks on surfaces with fuzz layers of different thicknesses. Arc current is 7 A [68].

To obtain the estimation relation (23), we used the thermal diffusivity of W-fuzz $a_f = 0.092$ cm^2 s^{-1} reported in [80]. In (22) and (23), the crater radius, the current, and the time are expressed in micrometers, amperes, and nanoseconds, respectively. If the W-fuzz thickness is larger than that determined by (23), the layer does not burn out completely, and the spot 'sticks' in it, i.e., it may return to the former place. Thus, so-called grouping of the spot cells occurs, and the spot's trajectory becomes 'entangled' (Fig. 7), while this is not the case with a small fuzz thickness [70–72]. As a result of the cell grouping, the velocity of the spot motion in the external tangential magnetic field decreases sharply, the track of the spot broadens, and traces of molten metal appear (Fig. 8).

Expressions (22), (23) include the current per spot cell. To estimate it, we will use the results of studying the structure of the track of a cathode spot moving in an external magnetic field in the case of a small thickness of the nanofiber layer, when there is no grouping of the cells (see Fig. 6). The choice of a small layer thickness is dictated by the fact that, first, the track width in this case is small enough to accurately determine the number of simultaneously operating spot cells and, second, since the nanofiber layer is almost completely destroyed during the operation of the cathode spot, a new cell cannot appear in the same place. In Fig. 6, individual craters are clearly visible in the spot track; their number varied from two to three along the track width, and the average crater size was a few micrometers. The track looks like a herringbone with separate branches, which indicates the division of the spot and the existence of individual cathode spots having an internal structure. The current per individual spot is approximately equal to the threshold current of the vacuum arc, i.e., to 1.5–2 A; hence, the current per spot cell can be estimated to range between 0.5 and 1 A. Direct counting of the number of simultaneously operating spot cells using high-speed photography yielded the same estimate of the current per spot cell (0.5–1 A) for a nanostructured layer 1 to 3 μm in thickness [75].

And, finally, a close estimate of the current per spot cell can be obtained taking into account the changes in erosion characteristics that occur when the thickness of the nanostructured surface layer becomes greater than 2 μm, as was found in the experiment described in [68]. The observed threefold increase in the erosion rate was due to the grouping of the cathode spot cells and the appearance of a liquid metal fraction in the spot. According to (23), such a grouping of spot cells is possible at $r_{crf} < l_d$, i.e., at currents of 0.9–1 A. The reason for the increase in erosion rate will be considered in Section 3.4.

A cell current of the order of 1 A allows us to estimate some parameters of the cathode spot. The radius of the crater should match the thickness of the fuzz layer. With its thickness of ~ 1 μm, the radius of an individual crater observed in experiments ranged from 0.8 to 1.3 μm [72]. For this fuzz thickness, the velocity of motion of a cathode spot cell in an external tangential magnetic field should be, according to (23), about 3.5×10^4 cm s^{-1}. The average velocity obtained experimentally is $\approx 1.5 \times 10^4$ cm s^{-1} [71]. The agreement with the experiment is quite good, considering that an actual cathode spot moves along a curvilinear trajectory.

3.4 Erosion characteristics of arc discharges with W-fuzz samples

From the viewpoint of using tungsten as a divertor material in thermonuclear facilities with magnetic plasma confinement, it is a critical challenge to have the arc discharge erosion products enter the thermonuclear plasma. According to (8), the rate of ion erosion of a fuzz, γ_{if}, is about 196 μg C^{-1}. For pure tungsten, we have $\gamma_{iW} \approx 125$ μg C^{-1}. In view of the cyclicity of the processes occurring in the cathode spot of a vacuum arc, a correction was introduced [1, 4, 5] to formula (8), which reduces the erosion rate for a pure tungsten cathode by 20–40%. Our estimation indicates that the rate of ion erosion of W-fuzz is higher than that of pure tungsten, despite the fact that its density is much lower. At the same time, it is approximately one third the total erosion rate measured for a nanostructured layer of small thickness. We have shown that a significant contribution to the erosion can be made by the mechanical destruction of nanofibers under the action of a plasma jet expanding from the sample [68].

The results of a study of the mass-charge composition of the arc plasma for W-fuzz cathodes are presented in [76]. It was found that, during about the first five pulses, when the main part of the fuzz layer burns out, ions with the lowest ionization potential, namely singly charged tungsten and carbon ions, are present in the arc plasma. Then, within about 10 pulses, the rest of the fuzz is destroyed. This region, in which the mean charge state of tungsten ions remains lower than that in the plasma of arcs with pure tungsten cathodes, can be called a transition region between the fuzz and the pure tungsten. Finally, starting from approximately the 15th pulse, the mean charge state of tungsten ions is close to that for a pure tungsten cathode. Figure 9 shows the mass-charge spectrum for the first pulse, when the arc operates directly on the fuzz surface. Let us analyze the obtained results. From formula (8) for the erosion rate, it is easy to obtain an expression for the mean charge state of an arc plasma [21, 22]:

$$Z \approx \frac{3 i_i m}{2 i_e e \rho} \left(\frac{\bar{h}_f}{a_f} \right)^{1/2}, \qquad (24)$$

where i_i is the ion current directed from cathode to anode [84], i_e is the electron current (arc current plus ion current), and m is the ion mass.

Substituting the parameters of the fuzz in (24), we obtain an estimation relation for the mean charge state number of tungsten ions in the arc plasma: $Z \approx 8 i_i / i_e$. The measurements reported in [83] showed that the values of i_i/i_e for ten different metals are in the range from 0.08 to 0.1. A wider spread in the values of i_i/i_e measured for metal cathodes, from 0.05 to 0.14, was obtained by the authors of [84]. Thus, it can be concluded that fuzz formation and the associated change in the physical and explosive emission properties of the cathode lead to a decrease in the mean charge state of tungsten ions in the arc plasma to +1, as was observed experimentally. As the fuzz is more and more destroyed from pulse to pulse, the mass-charge composition of the plasma ions gradually becomes similar to that characteristic of pure tungsten cathodes. The mean charge state number of tungsten ions increases from +1 to +3.

The experimentally found dependence of the mass-charge state composition of an arc plasma on the number of pulses is due to a change in the efficiency of ionization processes in the plasma. The mean charge state number of ions in a plasma can be determined as a function of density and temperature from the expression [85]

$$Z = \frac{A T^{3/2}}{n} \exp\left(-\frac{I(Z, n, T)}{T} \right), \qquad (25)$$

where Z is the mean charge state number of the ions, the factor $A = 6 \times 10^{21}$ cm^{-3} $eV^{-3/2}$, T is the plasma temperature, and n is the density of the plasma heavy component. For tungsten, the average ionization potential $I = I_0 - \Delta I$ as a function of mean ion charge state can be estimated, for ion charge numbers up to +3, as $I_0 = I_1 Z$, where $I_1 \approx 8$ eV is the first ionization potential. The correction $\Delta I = Ze^2/L_D$ is the decrease in ionization potential due to the Coulomb interaction in the region of weakly nonideal plasma and $L_D = [T/(4\pi Z^2 e^2 n)]^{1/2}$ is the Debye radius.

Figure 10 shows the mean charge state number of the W-cathode arc plasma as a function of the electron temperature for plasma densities of 10^{19} and 10^{20} cm^{-3}. The choice of these plasma densities was dictated by the fact that, in this range of densities, the charge composition of the arc plasma becomes settled, and then it 'freezes' [86]. Using the given plots, one can obtain an estimate of the plasma temperature depending on the mean charge state number, $T \sim Z$ [eV],

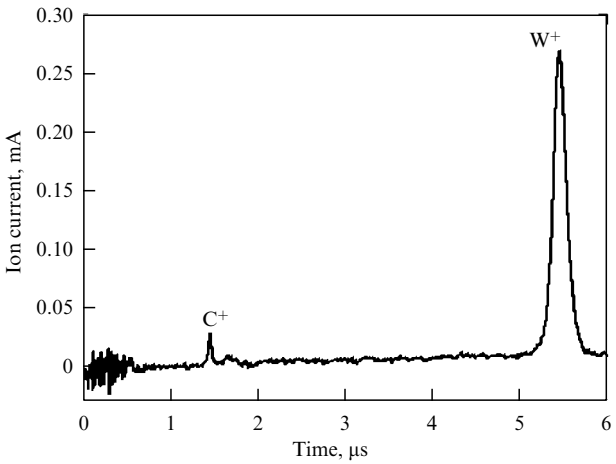

Figure 9. Typical mass-charge spectra of arc plasma for W-fuzz cathodes measured during the first arc pulses.

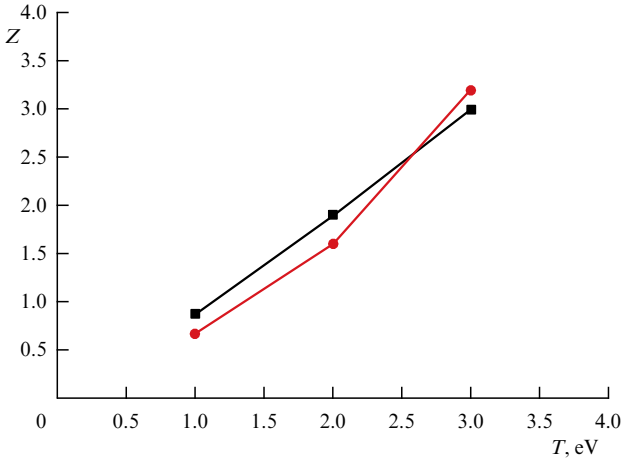

Figure 10. Temperature dependence of the mean charge state number of tungsten ions at a plasma density of 10^{19} (black) and 10^{20} (red) cm^{-3}.

which agrees with the results of calculations of the ionic composition of arc plasmas [87].

Based on the performed analysis of the mass-charge composition of the arc plasma, some conclusions can be drawn about the change in T_{cr} during the formation of fuzz on a tungsten surface. At a temperature close to T_{cr}, conductors explode [13]. The destruction of an exploding cathode microprotrusion starts at the top. However, as can be seen from Fig. 2, the temperature of the main part of the microprotrusion is also close to T_{cr}. It is obvious that, for a nanofiber structure, the binding energy of tungsten atoms and, accordingly, the critical temperature can be significantly lower than those for pure tungsten. This, in particular, is indirectly indicated by the intense erosion of W-fuzz cathodes. For pure tungsten, the estimates of T_{cr} obtained by various methods are in the range from 12,000 to 23,000 K [88]. These estimates exceed the electron temperature values we obtained for the mean charge state number +1 (first pulses). Hence, it can be concluded that the formation of fuzz reduces T_{cr} to about 1 eV. It should be noted that the decrease in T_{cr} has an insignificant effect on the earlier estimates, since $\bar{h}_f$ logarithmically depends on the critical temperature and, moreover, since the current action integral in relations (15) and (17) is to the inverse fourth power and under the square root, respectively. However, the change in T_{cr} must be taken into account when analyzing the heating of a cathode, particularly in the stage of formation of a liquid metal fraction.

Electrode erosion in the form of liquid metal droplets makes the largest contribution to the total erosion and may have, in principle, the most significant impact on thermonuclear plasma. As noted in Section 3.3, the formation of a liquid metal fraction, clearly visible in the track of the cathode spot (see Fig. 8), is induced by the grouping of cells at a nanostructured layer thickness of more than 2 μm. To analyze the processes responsible for the cell grouping, we use the solution of the heat equation with a moving boundary [85],

$$T(r) = T_{cr} \exp\left[-\frac{v_{fr}(r - r_{exf})}{a_f}\right]. \qquad (26)$$

When writing (26), it was assumed that a destruction wave propagates into the bulk cathode, with the temperature at the wave front $T(r_{exf}) = T_{cr}$ and the front velocity $v_{fr} = dr_{exf}/dt$. Taking into account the significant differences in the thermophysical properties between W-fuzz and pure tungsten, the boundary condition can be written as $T(l_d) = T_0$. In view of this boundary condition and the relationship between the wave propagation velocity and r_{exf} described as

$$v_{fr} \approx \frac{i_c^2}{16\pi^2 \bar{h}_f r_{exf}^3}, \qquad (27)$$

we can obtain the dependences of the destruction zone and melt zone radius on the nanostructured layer thickness l_d. For the latter case, the melt zone is defined by the condition $T(r_m) = T_m$. The plots of these dependences are given in Fig. 11 for two values of the initial temperature T_0. As can be seen from the plots shown in the figure, at a small W-fuzz thickness and $T_0 = 1000$ K, the nanostructured layer is almost completely destroyed due to Joule heating, and for a 1-μm-thick W-fuzz layer, the melt zone thickness is about 0.1 μm. The choice of the initial temperature equal to 1000 K

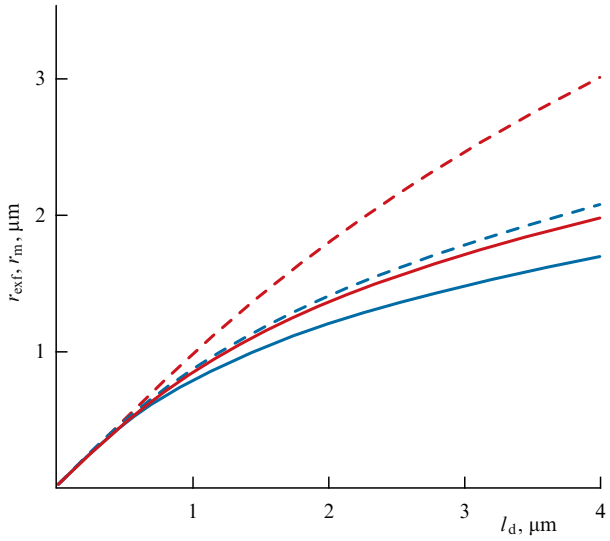

Figure 11. Dependences of the destruction zone radius r_{exf} (solid curves) and melt zone radius r_m (dashed curves) on nanostructured layer thickness. Blue curves correspond to $T_0 = 1000$ K, red curves, to $T_0 = 3000$ K.

was dictated by the conditions of experiments [68] that were carried out at this temperature of the plate. At short operation times of spot cells (shorter than 10 ns), the cells, driven by the magnetic field, move with high velocities over the surface, leaving behind craters with slightly melted nanofibers along the crater radius. The situation is different when the temperature increases due to the grouping of spot cells. The reasons for this increase in temperature are the following. First, the cell operation time increases; second, as noted in Section 3.3, the layer does not burn out completely and the spot may return to the place already heated, and, third, the surface is heated additionally due to the presence of other cells closely located.

To conclude this section, we consider the direct influence of the erosion processes that occur during unipolar arcing on the thermonuclear plasma. The calculations performed by the authors of [89] show that, when tungsten enters the plasma at a rate of more than 30 mg s^{-1}, the radiative losses can reach 60% of the energy heating the thermonuclear plasma. Taking into account that, in the case of spot cell grouping, the tungsten influx rate is 12 mg s^{-1} at a current of 7 A [68], the above threshold (30 mg s^{-1}) will be exceeded at a unipolar arc current of 25 A. This situation is quite real; in particular, in the experiment on studying unipolar arcs that was carried out on the PISCES-A facility [67], the arc current reached 80 A. At the same time, there are two factors that can moderate the detrimental effect of unipolar arcs. The first is that, as noted in Section 3.2, the higher the arc current, the lower the potential of the plate required to sustain the discharge due to the resistance of the plasma in contact with the plate. The second factor is that, as calculations have shown, the thickness of the nanostructured layer can be limited due to ELM plasma instabilities affecting its growth [90]. Thus, it can be concluded that the degree of influence of unipolar arcs on the course of thermonuclear reactions in thermonuclear facilities under development is currently open to question. Nevertheless, it is obvious that the problem does exist and needs a further detailed study.

4. Initiation of a vacuum breakdown in the accelerating structures of electron–positron colliders

4.1 Criteria for the initiation of a radiofrequency vacuum breakdown

Interest in studying the mechanism of radiofrequency vacuum breakdowns arose in connection with the progress in high-power microwave electronics [7]. Investigations have shown that an obstacle to increasing microwave energy is the so-called effect of microwave pulse shortening, due to which an increase in power leads to a decrease in pulse duration, and the generated microwave energy is not over several ten joules [91]. The main cause of this effect is the radiofrequency vacuum breakdown of the resonators and slow-wave structures of microwave generators. Recently, studying the mechanism of radiofrequency vacuum breakdowns has also become relevant in connection with the development of linear electron–positron colliders, which are associated with further progress in elementary particle physics. To achieve high luminosity with the colliders, the energy of colliding particles must be as high as several teraelectronvolts. This is the goal in developing the CLIC facility at CERN [92, 93]. Since the particles (electrons and positrons) are light, to avoid energy losses for radiation, the accelerated particles must move along a linear rather than a circular path, as they do in the Large Hadron Collider. The maximum voltage generated by DC voltage sources is on the level of several megavolts; therefore, the method of particle acceleration by radiofrequency electromagnetic waves was chosen. As a result, an accelerating gradient of the order of 100 MV m^{-1} was achieved. However, even with such a high gradient, the length of the accelerating structure for each type of particle should be more than 20 km. The main factor limiting the magnitude of the accelerating field is the vacuum breakdown developing from the surface of the accelerating structure [94]. In addition to the above-mentioned magnetic fields induced by emission currents and the absorption of the electromagnetic wave energy during a radiofrequency breakdown, the breakdown-induced change in the surface morphology of the accelerating structure significantly increases the probability of repeated breakdown initiation at the same place during the next accelerating pulse [95, 96].

The CLIC accelerating structure, designed to operate in the X-band, namely at 11.994 GHz, will be made of copper. One of the main requirements for the accelerating structure is that, at a 100-MV-m^{-1} accelerating gradient, the breakdown rate per pulse per m of the accelerating structure must be less than 3×10^{-7} [93]. The breakdown rate (BDR) is the probability of breakdown initiation in a given pulse; it is determined experimentally by dividing the number of breakdowns by the total number of pulses. In view of this requirement, experimental studies of the radiofrequency vacuum breakdown were mainly aimed at studying the breakdown statistics and the feasibility of electrode conditioning by pulses of electromagnetic waves. The study of the breakdown rate for accelerating structure prototypes has shown that the breakdown occurs spontaneously and uncontrollably; before its development, the structure is exposed without breakdown to tens to hundreds of thousands of pulses [96]. It has been found in [95, 96] that there are two types of breakdowns: a 'normal breakdown' (NL-BD), which occurs after the action of many pulses without breakdowns, and a 'following-pulse breakdown' (FP-BD), which occurs during the first pulse following the breakdown pulse. It turns out that there is a spatial relationship between FP-BDs and NL-BDs: they occur in almost the same place. It is obvious that the conditions for the FP-BD initiation arose as a result of the breakdown having occurred during the previous pulse. Therefore, it was concluded that the efficiency of the conditioning process is determined by the total number of electromagnetic wave pulses rather than by the number of breakdowns [97]. For a large number of pulses, the NL-BD development times are uniformly distributed over the duration of the electromagnetic wave pulse, while FP-BDs occur mainly at the beginning of the pulse. Examination of the statistics of radiofrequency (RF) vacuum breakdowns and vacuum breakdowns that occurred at a DC diode voltage [96] suggests that there is a common mechanism for these types of breakdowns.

As a result of a large number of experiments, two criteria for the development of vacuum breakdowns in radiofrequency fields have been found. The first one relates the breakdown rate and the electric field amplitude E_A:

$$\frac{E_A^{30}}{\mathrm{BDR}} = \mathrm{const}\,, \tag{28}$$

and the second one relates E_A and the pulse duration t_p at a constant BDR:

$$E_A t_p^{1/6} = \mathrm{const}\,. \tag{29}$$

In view of (28) and (29), we obtain an expression relating the three quantities, E_A, τ_p, and BDR [98]:

$$\frac{E_A^{30}\tau_p^5}{\mathrm{BDR}} = \mathrm{const}\,. \tag{30}$$

4.2 Microexplosive processes in a radiofrequency vacuum breakdown

To analyze the processes involved in a radiofrequency vacuum breakdown, we start with an investigation of the microexplosive processes initiated on electrodes by gigahertz electromagnetic waves. For this purpose, calculations were carried out using the system of equations (9)–(13) that were solved with the voltage in the electric circuit specified as [27]

$$U_{\mathrm{out}}(t) = U_0 \sin(\omega t)\,, \quad \sin(\omega t) > 0\,,$$
$$U_{\mathrm{out}}(t) = 0\,, \quad \sin(\omega t) < 0\,, \tag{31}$$

where $\omega = 2\pi\nu$ with frequency $\nu = 12$ GHz.

Figure 12 shows the calculated time dependence of the load voltage during the explosion of a cathode microprotrusion at a radiofrequency circuit voltage. The plot shown in Fig. 12 makes it possible to estimate the current action integral for this case $\bar{h} = j^2\tau/4 = 2.9 \times 10^9$ A^2 s cm^{-4}, where $\tau \approx 9.6$ ns is the delay time to the explosion and $j = 1.1 \times 10^9$ A cm^{-2} is the current density at a peak voltage across the gap. Thus, according to the calculations, the value of the current action integral changes slightly when going from DC to RF voltage.

Subsequent investigations of the behavior of the current action integral have shown that its value decreases a little with a decrease in current density, which, however, is also characteristic of cases with a DC voltage. At the moment of explosion, the voltage U_{load} reaches 100 V and then stabilizes

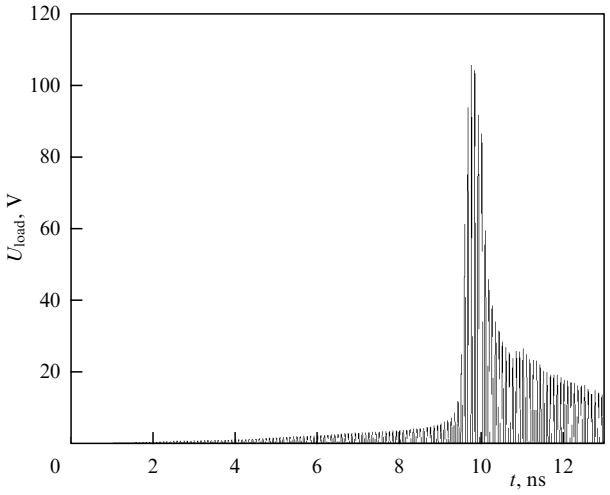

Figure 12. Time dependence of load voltage U_{load} for radiofrequency circuit voltage determined by formula (31) with $U_0 = 3200$ V (3.2-A current amplitude); $r_c = 0.3$ μm.

at a level of about ≈ 10 V. The quantity U_{load} is the resistive voltage drop that occurs during the current flow through the metal–plasma contact and the cathode plasma region under calculation. Accordingly, during the explosion of a cathode microprotrusion, the power density, jU_{load}, reaches tens of watts per square micrometer. The electromagnetic wave is the only source of energy absorbed by the microprotrusion during the explosion. Apparently, this accounts for the 'missing energy' effect that was observed in the experiment on studying the radiofrequency vacuum breakdown in CLIC accelerating structures [94].

Figure 13 shows material density distributions in the post-explosion phase for the cases of DC and RF voltage. As can be seen from the figure, these distributions are almost identical. This accounts for the common nature of the surface damage (micrometer-size craters) caused by DC and RF vacuum breakdowns. Thus, it can be concluded that the parameters of microexplosive cathode processes do not change in going from a DC to an RF electric field.

4.3 Explosive emission model of a radiofrequency vacuum breakdown

Before investigating the parameters responsible for the initiation of explosive electron emission in a radiofrequency vacuum breakdown, we consider the results of a study of DC vacuum breakdown reported in [99]. The authors of [99] used the same cathode material and cathode treatment techniques as those used in the study of the radiofrequency breakdown in CLIC accelerating structures [94].

In the experiment described in [99], both electrodes were made of pure copper (Cu OFE, UNS C10100). A rounded rod 2.3 mm in diameter served as the anode, and the grounded cathode was a 10×50-mm plate. The electrode gap spacing d was varied from 10 to 50 μm; most of the shots were carried out at $d = 20$ μm. The breakdown electric field and the field enhancement factor, which was determined from the Fowler–Nordheim characteristics, were investigated. Their values were obtained in the 'conditioning' mode, when the number of breakdowns was counted at a DC voltage. In addition, the breakdown delay time and threshold voltage were investigated. The voltage pulse duration was 1–2 s with a rise time of 100 ns. Below, we will use the following average values of the vacuum breakdown characteristics obtained in [99]: average field enhancement factor during breakdown $\beta = 77$, average breakdown field $\beta E_{av} = 10.8$ GV m^{-1}, and average breakdown delay time (minus the diode voltage rise time) $t_d \approx 50$ ns.

The studies of pulsed vacuum breakdown [4–6] have shown that, at high electric fields at the cathode, the exponential field dependence of the breakdown initiation delay time becomes a power dependence, $t_d \propto E_{av}^3$, where E_{av} is the macroscopic field at the cathode. For plane electrodes, we have $E_{av} = U/d$, where U is the diode voltage and d is the electrode gap spacing. The change in the dependence of the delay time on the electric field strength is because of the influence of the space charge of emitted electrons, due to which the emission current density obeys the '3/2 power' law [6]

$$j_{3/2} = \frac{1}{9\pi}\left(\frac{2e}{m_e}\right)^{1/2}\frac{U^{3/2}}{d_{eff}^2}\,, \tag{32}$$

where e and m_e are, respectively, the electron charge and mass. The effective gap spacing is determined as $d_{eff} = U/(\beta E_{av})$, where β is the factor of field enhancement at cathode microprotrusions.

To calculate the electric field at the top of a microprotrusion taking into account the space charge of emitted electrons, E_0, we use the one-dimensional approximation, as the space charge of emitted electrons is localized at distances of the

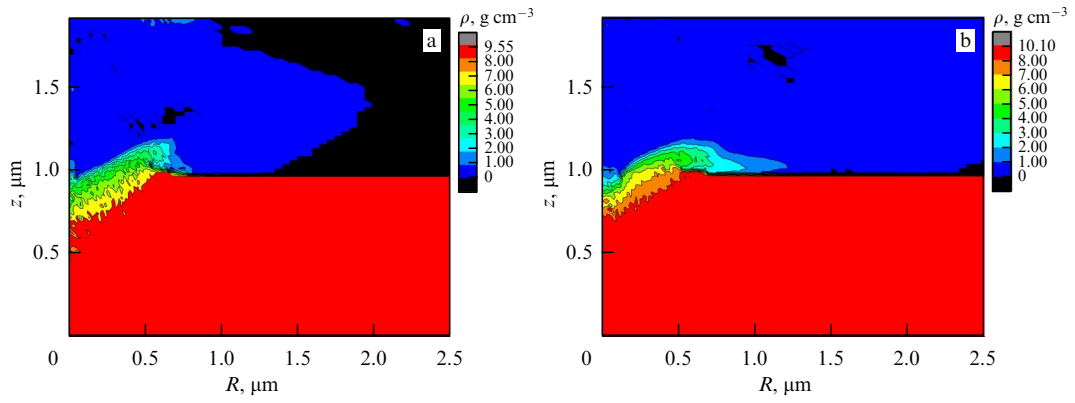

Figure 13. Material density distribution in the post-explosion phase for (a) an RF ($t = 10$ ns) and (b) a DC ($t = 3$ ns) circuit voltage. Calculation parameters are the same as in Fig. 12.

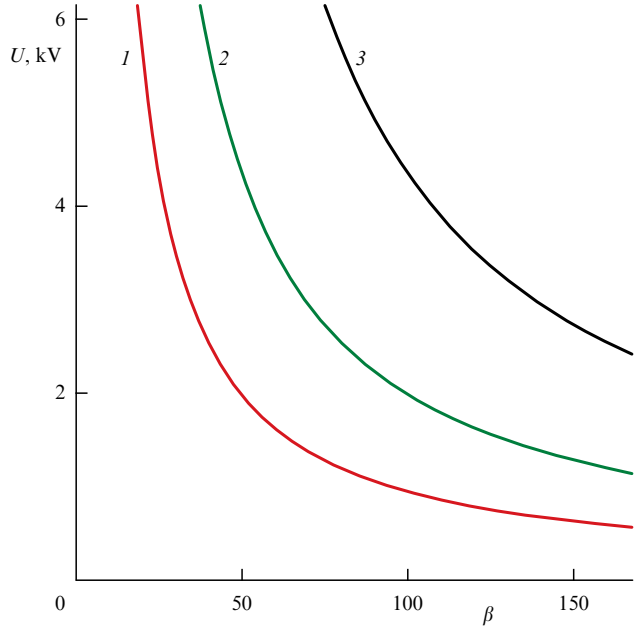

Figure 14. Dependence of breakdown voltage U on the field enhancement factor at a breakdown delay time of 50 ns for different gap spacings: $d = 10$ μm (*1*), 20 μm (*2*), and 40 μm (*3*).

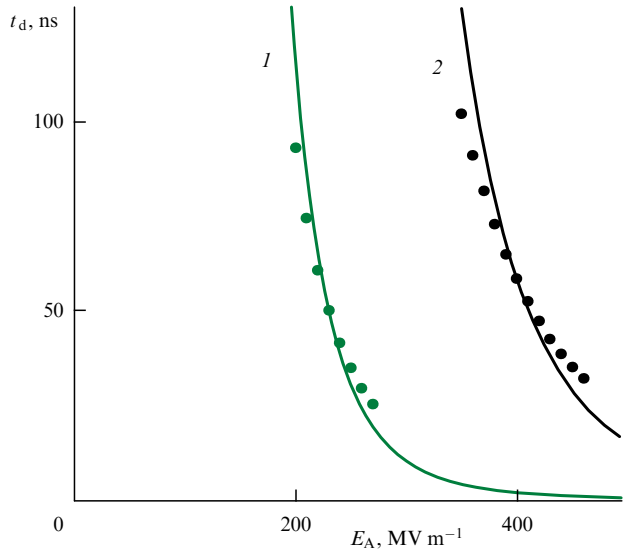

Figure 15. Dependence of the breakdown delay time t_d on electric field amplitude E_A on the surface of an accelerating structure for $\beta = 77$ (*1*) and $\beta = 50$ (*2*). Curves represent relation $t_d \propto E_A^{-6}$.

order of 10^{-6} cm from the emission boundary [100]. The equation for finding the electric field at the microprotrusion top is written as

$$4kU^{3/2}\exp\left(-\frac{B}{E_0}\right)-3U=9k^2A^2E_0^2d_{\text{eff}}^2\exp\left(-\frac{2B}{E_0}\right)-3E_0d_{\text{eff}}\,, \tag{33}$$

where A and B are the coefficients in the Fowler–Nordheim equation $j_{\text{FN}} = AE_0^2\exp(-BE_0)$ and $k = 2\pi(2m_e/e)^{1/2}$.

Figure 14 shows plots of the dependence of the diode breakdown voltage on the field enhancement factor β for different electrode gap spacings. The given plots were obtained with the use of expression (4) with $\bar{h} = 3.1\times 10^9$ A^2 s cm^{-4} and $t_d = 50$ ns. The electric field entering in the Fowler–Nordheim equation was calculated using expression (33). As can be seen from Fig. 14, for the conditions of the experiment [99], the quantity βE_{av} varies in the range from 11.5 GW m^{-1} (at $U = 6$ kV) to 10 GW m^{-1} (at $U = 2$ kV) irrespective of the electrode gap spacing, which is in quite good agreement with experimental data, giving virtually the same threshold value of the field enhancement factor as that reported in [100]: $\beta = 48$ (see curve *2* in Fig. 14) for the macroscopic field on the cathode surface $E_{\text{av}} = 225$ MV m^{-1}. Thus, the simplest estimates based on the results of investigations of pulsed vacuum breakdown describe quite well the experimental data on the DC breakdown for the materials used in CLIC accelerating structures. Next, we use the obtained results to consider the processes leading to the initiation of explosive electron emission in radiofrequency vacuum breakdowns.

In what follows, we analyze the empirical relations (28) and (29). Obviously, (28) reflects a sharp increase in the breakdown probability with an increase in electric field amplitude. Relation (29) should reflect the relationship between E_A and the time of breakdown initiation. It implies that a breakdown is possible within a radiofrequency pulse if the time of its initiation is less than the pulse duration: $t_d \leqslant t_p$.

For 'normal breakdowns' (NL-BD), these times are uniformly distributed over the pulse duration [96]. Since the delay time is related to the field enhancement on the surface of the accelerating structure, its maximum value $t_d \approx t_p$ must correspond to the minimum value of the field enhancement factor at which breakdown is possible, $\beta_{\text{threshold}}$. Empirical relation (29) implies that, with such a relationship between electric field and pulse duration, $\beta_{\text{threshold}}$ remains unchanged; that is, the conditions for breakdown initiation do not change and a breakdown occurs at $\beta \geqslant \beta_{\text{threshold}}$. Violation of this relationship would lead to a change in $\beta_{\text{threshold}}$ and, as a consequence, to a change in BDR, in view of its strong field dependence [see relation (28)].

A simulation of the heating of a cathode microprotrusion by the thermal field emission current under the action of an alternating electric field of frequency 10 GHz is presented in [101]. It should be noted that the application of classical emission formulas to the case of electric fields varying in the gigahertz range is justified due to the fact that the electron tunneling time of 10^{15} s [102] is two orders of magnitude shorter than the electric field oscillation period. In simulation [101], the space charge of emitted electrons was not taken into account; therefore, quantitative estimates of the breakdown initiation parameters based on the calculations would be incorrect. Nevertheless, an important result of the simulation is that a relationship between the cathode heating time to the melting point, t_m, and the current density averaged over the oscillation period was found to be $j_{\text{av}}^2 t_m = \text{const}$, indicating that the main source of heat release in a cathode microprotrusion is its resistive heating by the emission current. This relationship did not depend on the frequency in the gigahertz range if no breakdown occurred within the first oscillations of the electric field.

Taking into account the results of this simulation, we estimate the relation between the delay time and the macroscopic field at the cathode at a field oscillation frequency lying in the 10-GHz range, for which we will use (4) with j replaced by j_{av}. Consider a diode with plane electrodes, having parameters similar to those used in [100], to which a voltage $U = U_A \sin(\omega t)$ is applied. We choose the

voltage amplitude so that the maximum macroscopic field at the cathode, $E_A = U_A/d$, is several hundred megavolts per meter. The effect of the space charge of emitted electrons will be taken into account according to the procedure described above for a DC electric field.

The calculation results are shown in Fig. 15. The calculations were performed for the field enhancement factor $\beta = 77$, equal to the average value obtained in [99], and, for comparison, for $\beta_{\text{threshold}} = 50$, approximately equal to the threshold value.

The expected operating parameters of the CLICK accelerating structure are: the radiofrequency pulse duration at a field gradient of 100 MV m^{-1} is 156 ns, the full pulse duration is 240 ns, and the maximum electric field on the surface is less than 260 MV m^{-1} [94]. According to the plots shown in Fig. 15, with a surface field of 250 MV m^{-1} and a radiofrequency pulse duration of 150 ns, breakdown is possible at $\beta > \beta_{\text{threshold}} \approx 70$. The typical values of β for the copper electrodes used in accelerating structures range between 30 and 60 [95, 103]. These values were obtained using the Fowler–Nordheim characteristics for a DC mode at low emission currents. We, however, are interested in values of β immediately before the breakdown-initiating pulse. It is natural to suppose that, for a breakdown to be initiated, microirregularities must exist on the cathode surface whose field enhancement factors, in accordance with our estimates, would exceed the typical values of β corresponding to no breakdown cases.

We emphasize that $\beta_{\text{threshold}} \approx 70$ is the minimum value of the field enhancement factor at which $t_d \approx t_p$; that is, a significant proportion of the breakdowns detected in experiments was initiated at microirregularities with much greater β. This is especially true for FP-BDs [95], which occur mainly in the initial phase of a radiofrequency pulse. The formation of such microirregularities during FP-BDs is obviously associated with the appearance of the liquid-metal phase of the cathode spot, the extrusion of which from the melt zone leads to the formation of new explosive emission centers [8, 19]. The calculation results given in Fig. 15 are also in good agreement with the empirical relation (29): $t_d(\beta_{\text{threshold}}) \approx t_p \propto E_A^{-6}$.

4.4 Simulation of prebreakdown processes

The considered simplest model of the initiation of radiofrequency vacuum breakdown, providing some agreement with experimental data, does not present a rigorous quantitative description of the characteristics of a radiofrequency breakdown. In view of this, a model was developed that self-consistently takes into account the heating of a cathode microprotrusion, the emission of electrons, and the effect of the space charge of emitted electrons [104, 105].

The effect of the space charge of emitted electrons was taken into account by solving the Poisson equation written in cylindrical coordinates

$$\Delta U(r,z) = -4\pi\rho_e(r,z)\,, \tag{34}$$

where ρ_e is the space charge of emitted electrons. Equation (34) was solved by the particle-in-cell method.

The field emission current density was calculated in the Miller–Good approximation [106]:

$$j_{FE} = \frac{4\pi me}{h^3}\int_0^\infty \mathrm{d}\varepsilon \int_0^\varepsilon \mathrm{d}\varepsilon_n f_{FD}(\varepsilon) D\left(E_c,\varepsilon_n\right), \tag{35}$$

where $D(E_c,\varepsilon_n)$ is the transparency of the potential barrier at the metal–vacuum interface, E_c is the electric field strength on the microprotrusion surface, f_{FD} is the Fermi–Dirac function describing the energy distribution of electrons in the metal, $\varepsilon = (\hbar k)^2/(2m)$ is the energy of the electrons having the wave vector $\mathbf{k}$ in the metal, $\varepsilon_n = (\hbar k_n)^2/(2m)$ is the energy of the electrons moving along the normal to the potential barrier, and $\hbar = h/(2\pi)$ is Plank's constant. According to the Miller–Good approximation, we have

$$D(E_c,\varepsilon_n) = \left[1+\exp\left(Q(E_c,\varepsilon_n)\right)\right]^{-1}, \quad \varepsilon_n < \varepsilon_L\,,$$

$$D(E_c\,,\varepsilon_n) = 1\,, \quad \varepsilon_n > \varepsilon_L\,, \tag{36}$$

$$Q(E_c,\varepsilon_n) = \frac{4\sqrt{2}}{3}\left(\frac{m^2e^5}{\hbar^4E_c}\right)^{1/4} y^{-3/2}v(y)\,, \tag{37}$$

$$y = \frac{\sqrt{e^3E_c}}{|\varepsilon_F+\varphi-\varepsilon_n|}\,, \tag{38}$$

where $\varepsilon_L = \varepsilon_F + \varphi - \sqrt{e^3E_c/2}$ is the height of the potential barrier for the electrons, and $v(y)$ is the work function; the function φ is determined by elliptic integrals [107].

The heating of the microprotrusion by the emission current was taken into account using the two-temperature (electrons and phonons) system of heat equations [4]

$$\rho c_e(T_e)\frac{\partial T_e}{\partial t} = \nabla\left(\lambda_e(T_e,T_p)\,\nabla T_e\right) - G(T_e-T_p) + \kappa(T_p)j^2\,, \tag{39}$$

$$\rho c_p(T_p)\,\frac{\partial T_p}{\partial t} = \nabla\left(\lambda_p(T_p)\nabla T_p\right) + G(T_e-T_p)\,, \tag{40}$$

with the boundary and initial conditions

$$-\lambda_e(T_e,T_p)\nabla T_e\big|_S = q_{\text{Nott}}, \quad T_{e,p}(r,z,t)\big|_{z=0} = T_0\,,$$
$$T_{e,p}(r,z,0) = T_0\,. \tag{41}$$

Here, $c_e(c_p)$ and $\lambda_e(\lambda_p)$ are the heat capacity and heat conductivity of the electron (phonon) subsystem, respectively; G is the electron–phonon coupling coefficient, which determines the rate of energy exchange between electrons and phonons; κ is the resistivity of the microprotrusion material; T_0 is the initial temperature; and q_{Nott} is the energy released on the surface due to the Nottingham effect:

$$q_{\text{Nott}} = \frac{4\pi m}{h^3}\int_0^\infty \mathrm{d}\varepsilon \int_0^\varepsilon \mathrm{d}\varepsilon_n\,(\varepsilon-\mu) f_{FD}(\varepsilon) D(E_c,\varepsilon_n)\,, \tag{42}$$

where μ is the chemical potential at T_e.

The distribution of the current inside the microprotrusion, $j = -\kappa^{-1}\nabla U$, was calculated by solving the Laplace equation with the boundary condition on the surface $\nabla U|_S = \kappa j_{em}$.

The two-temperature (electrons and lattice) model was used in the calculations, since the energy released in the microprotrusion heated by the emission current due to both sources (Nottingham and Joule effects) enters the electronic subsystem and then is transferred to the lattice [4]. Thus, in the general case, the electron temperature becomes 'separated' from the lattice temperature. The higher the emission

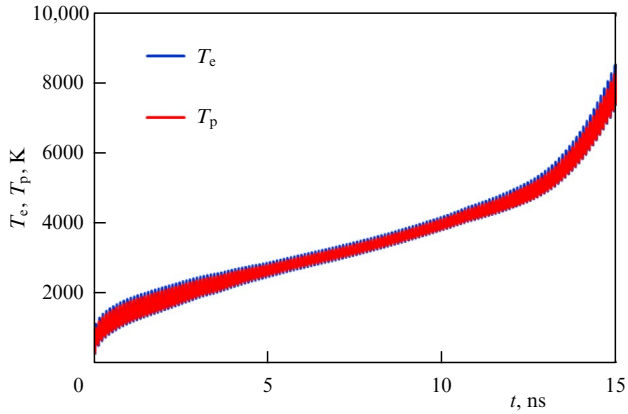

Figure 16. Dependences of the maximum temperatures of electrons (blue curve) and the lattice (red curve) on radiofrequency pulse duration. Calculation parameters: electric field amplitude on the surface, $E_A = 300$ MV m^{-1}, $T_0 = 300$ K, $\beta \approx 65$ (microprotrusion tip radius $r_{mp} = 22.5$ nm, height $h_{mp} = 2$ μm, and cone half-angle $\alpha = 3°$); $G = 4 \times 10^{17}$ W m^{-3} K^{-1}.

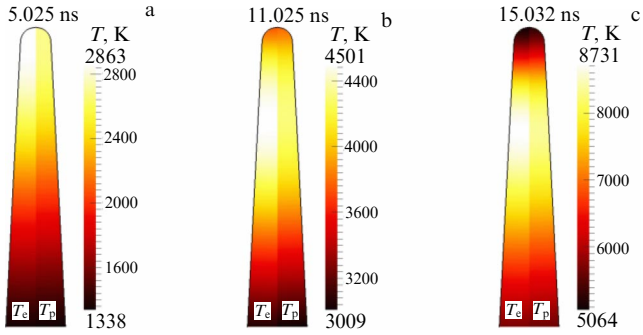

Figure 17. Two-dimensional profiles of electron temperature T_e and lattice temperature T_p (right) at the microprotrusion tip (between $z = h_{mp}$ and $z = h_{mp} - 20r_{mp}$) for time points (a) 5.025, (b) 11.025, and (c) 15.032 ns. Calculation parameters are the same as in Fig. 16.

current density, the greater the difference between the electron and phonon temperatures. The difference between the electron and phonon temperatures results in so-called high-frequency electron heat conduction, such that part of the energy entering the electronic subsystem is not transferred to phonons but is removed into the bulk microprotrusion [108].

The calculations were carried out for a conical microprotrusion with a tip radius of several ten nanometers, height of 1–2 μm, and cone angle of up to 10 deg. The electric field enhancement factor β was determined from the solution of the Laplace equation; its value was varied by varying the geometrical parameters of the microprotrusion. In all calculation runs, the electric field amplitude was 300 MV m^{-1} and the frequency was 10 GHz. The time of initiation of explosive electron emission was assumed to be the time at which the lattice became heated to $T_{cr} = 8390$ K.

The variations in electron and phonon temperatures are shown in Figs 16 and 17. Let us briefly dwell on the physical processes responsible for this behavior of the temperatures. The effect of the space charge of emitted electrons has the result that, at the time zero, the maximum electric field at the microprotrusion tip is approximately half that obtained from the solution of the Laplace equation. The electric field is more evenly distributed over the tip and its adjacent region. Here, the initial increase in temperature is caused by heating due to the Nottingham effect; the electron and phonon temperatures

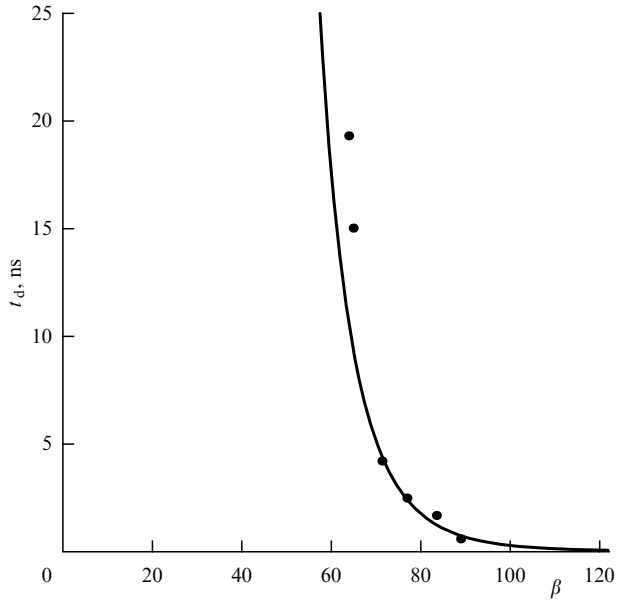

Figure 18. Dependence of the breakdown delay time on field enhancement factor β. Electric field amplitude at the cathode $E_A = 300$ MV m^{-1}. Dots: simulation results; curve: $t_d \propto (\beta E_A)^{-6}$.

quickly reach values close to the inversion temperature above which the Nottingham effect becomes cooling. As the tip is heated, the thermal addition to the field emission current is compensated by a decrease in the electric field, which enhances tip cooling due to the Nottingham effect, while the further increase in temperature slows down sharply, and the maxima of the electron and phonon temperatures move into the bulk microprotrusion. As this movement progresses, the emission current density at the tip also decreases, since the field is screened by the beam of electrons emitted from the peripheral part of the microprotrusion. The electron emission from this microprotrusion part increases the total emission current, thereby increasing the current density over the microprotrusion cross section and the energy released due to Joule heating. As a result, the temperature reaches a maximum at a distance of several ten r_{mp} from the tip, where cooling due to the Nottingham effect is not substantial. The temperature of a significant part of the microprotrusion adjacent to its tip exceeds the melting and boiling points of copper as early as the 5th and the 11th nanosecond, respectively.

Figure 18 shows the calculated time of heating of the microprotrusion to the critical point as a function of the factor β. As can be seen from this figure, the relation $t_d \propto (\beta E_A)^{-6}$ holds at large β, and then t_d sharply increases, and at $\beta = 60$ the phonon and electron temperatures reach stationary values below T_{cr}. Accordingly, the simulation predicts the threshold microscopic field at which a radiofrequency vacuum breakdown will develop: $\beta E_A \approx 18$ GV m^{-1}. The above estimations performed using the current action integral gave approximately the same value of βE_A (≈ 17.5 GV m^{-1}).

Thus, the estimations and calculations performed for the processes involved in a radiofrequency vacuum breakdown allow us to assert with confidence that this type of breakdown, like a nanosecond pulsed vacuum breakdown, occurs due to explosive emission processes. Associated effects also observed during radiofrequency breakdowns are an increase in emission current and similar traces of surface damage such as micrometer-sized craters. The absorption of the electro-

magnetic wave energy during microexplosive processes occurring on the electrode surface in a radiofrequency vacuum breakdown gives rise to the 'missing energy' effect, such that the energy of the wave propagating in the electrode is lower than the energy of the incident and reflected waves. A distinctive feature of a radiofrequency vacuum breakdown is the presence of an alternating magnetic field, which is responsible for additional heating of the electrodes. Stressful changes in the electrode surface structure and local heating of some surface sections may significantly increase the probability of breakdown. In particular, we have shown that, when the surface microprotrusions are heated to 1000 K, the breakdown probability may increase by more than an order of magnitude, all other conditions being equal [105].

5. Conclusion

The estimates and the numerical simulation results presented in the paper, in our opinion, quite convincingly testify in favor of the explosive nature of the processes that occur during radiofrequency vacuum breakdowns and unipolar arcing in thermonuclear facilities with magnetic plasma confinement. The use of simple estimation procedures based on the analogy between the phenomena of explosive electron emission and electrical explosion of conductors is an effective way of analyzing and interpreting experimental data. The main cause of the occurrence of explosive emission processes is the changes in the structure and properties of the surfaces exposed to electromagnetic waves and helium plasma. However, whereas in the second case these changes are large-scale and easily observable, in the first case they are local, and their cause remains the subject of discussion. The surface changes may occur due to the heating of surface irregularities by an alternating magnetic field, dislocations piling up, surface melting, etc. [105, 109–112]. The complexity of studying the cause of the initiation of explosive emission processes on a surface exposed to electromagnetic waves is associated with the spontaneous and uncontrolled development of the breakdown. Moreover, there is a combination of many factors, in addition to those mentioned above, such as nonideal vacuum conditions, evaporation of impurities and copper atoms from the surface, and electron emission (dark current), that may lead to a breakdown. Significant progress in this matter can be achieved only by developing an experimental technique for studying radiofrequency vacuum breakdowns, which would make it possible to strictly control the emission processes, surface structure and temperature, and vacuum conditions.

This work was supported by the Russian Science Foundation (grant no. 20-19-00323). In Sections 2 and 3.4, results obtained with support from the Russian Foundation for Basic Research (grant no. 20-08-00378) are used. The authors are grateful to I V Uimanov, E V Oreshkin, and M M Tsventoukh for the calculations of the prebreakdown and microexplosive processes, and ionization processes in arc plasmas, and also to S Kajita and D Hwangbo for their kind permission to use the results of experiments with W-fuzz samples and for many years of fruitful cooperation.

References

1. Mesyats G A *J. Nucl. Mater.* **128–129** 618 (1984)
2. Mesyats G A, in *High Power Microwave Generation and Applications: Proc. of the Course and Workshop, Varenna, Italy, 9–17 September, 1991* (Eds D Akulina, E Sindoni, C Wharton) (Bologna, Italy: Publ. for the Società Italiana di Fisica by Editrice Compositori, 1992) p. 345
3. Mesyats G A "Issledovaniya po generirovaniyu nanosekundnykh impul'sov bol'shoi moshchnosti" ("Investigations on the generation of nanosecond high-power pulses"), Doctoral Thesis in Engineering (Tomsk: Tomsk Polytechnical Institute, 1966)
4. Bugaev S P et al. *Sov. Phys. Usp.* **18** 51 (1975); *Usp. Fiz. Nauk* **115** 101 (1975)
5. Litvinov E A, Mesyats G A, Proskurovskii D I *Sov. Phys. Usp.* **26** 138 (1983); *Usp. Fiz. Nauk* **139** 265 (1983)
6. Mesyats G A, Proskurovsky D I *Pulsed Electrical Discharge in Vacuum* (Berlin: Springer, 1989)
7. Mesyats G A *Pulsed Power* (Berlin: Springer Science and Business Media, 2007)
8. Mesyats G A *Cathode Phenomena in a Vacuum Discharge: the Breakdown, the Spark, and the Arc* (Moscow: Nauka Publ., 2000); Translated from Russian: *Ektony v Vakuumnom Razryade: Proboi, Iskra, Duga* (Moscow: Nauka, 2000)
9. Kartsev G K et al. *Sov. Phys. Dokl.* **15** 475 (1970); *Dokl. Akad. Nauk SSSR* **192** 309 (1970)
10. Mitterauer J et al., in *Proc. VII Intern. Symp. on Discharges and Electrical Insulation in Vacuum* (Novosibirsk: USSR, 1976) p. 83
11. Fursey G N *IEEE Trans. Electr. Insul.* **EI-20** (4) 659 (1985)
12. Anderson G W, Neilson F W, in *Exploding Wires* (Eds W G Chace, H K Moore) (New York: Plenum Press, 1962)
13. Oreshkin V I, Baksht R B *IEEE Trans. Plasma Sci.* **48** 1214 (2020)
14. Mesyats G A *IEEE Trans. Plasma Sci.* **23** 879 (1995)
15. Mesyats G A *Phys. Usp.* **38** 567 (1995); *Usp. Fiz. Nauk* **165** 601 (1995)
16. Mesyats G A *IEEE Trans. Plasma Sci.* **41** 676 (2013)
17. Shmelev D L, Barengolts S A *IEEE Trans. Plasma Sci.* **41** 1959 (2013)
18. Barengolts S A, Shmelev D L, Uimanov I V *IEEE Trans. Plasma Sci.* **43** 2236 (2015)
19. Barengolts S A et al. *J. Appl. Phys.* **129** 133301 (2021)
20. Kesaev I G *Katodnye Protsessy Elektricheskoi Dugi* (Cathodic Processes of an Electric Arc) (Moscow: Nauka, 1968)
21. Barengolts S A, Mesyats G A, Shmelev D L *J. Exp. Theor. Phys.* **93** 1065 (2001); *Zh. Eksp. Teor. Fiz.* **120** 1227 (2001)
22. Mesyats G A, Barengol'ts S A *Phys. Usp.* **45** 1001 (2002); *Usp. Fiz. Nauk* **172** 1113 (2002)
23. Oreshkin V I et al. *Phys. Plasmas* **11** 4771 (2004)
24. Oreshkin V I et al. *Phys. Plasmas* **23** 122107 (2016)
25. Slivkov I N *Elektroizolyatsiya i Razryad v Vakuume* (Electrical Isolation and Discharge in Vacuum) (Moscow: Atomizdat, 1972)
26. Barengolts S A et al. *Phys. Rev. Accel. Beams* **21** 061004 (2018)
27. Barengolts S A et al. *IEEE Trans. Plasma Sci.* **47** 3406 (2019)
28. Tkachenko S I et al. *High Temp.* **39** 674 (2001); *Teplofiz. Vys. Temp.* **39** 728 (2001)
29. Khishchenko K V et al. *Int. J. Thermophys.* **23** 1359 (2002)
30. Loskutov V V, Luchinskii A V, Mesyats G A *Sov. Phys. Dokl.* **28** 654 (1983); *Dokl. Akad. Nauk SSSR* **271** 1120 (1983)
31. Bushman A V et al. *Sov. Phys. Dokl.* **35** 561 (1990); *Dokl. Akad. Nauk SSSR* **312** 1368 (1990)
32. Shmelev D L, Litvinov E A *IEEE Trans. Plasma Sci.* **25** 533 (1997)
33. Shmelev D L, Litvinov E A *IEEE Trans. Dielectr. Electr. Insul.* **6** 441 (1999)
34. Oreshkin E V et al., in *7th Intern. Congress on Energy Fluxes and Radiation Effects, EFRE 2020, September 14–26, 2020, Tomsk, Russia* (Tomsk: Publ. House of IAO SB RAS, 2020) p. 408
35. Oreshkin V I, Barengolts S A, Chaikovskii S A *Tech. Phys.* **52** 642 (2007); *Zh. Tekh. Fiz.* **77** (5) 108 (2007)
36. Robson A E, Thonemann P C *Proc. Phys. Soc.* **73** 508 (1959)
37. Zykova N M, Nedospasov A V, Petrov V G *High Temp.* **21** 600 (1983); *Teplofiz. Vys. Temp.* **21** 778 (1983)
38. Tien J K et al. *J. Nucl. Mater.* **76–77** 481 (1978)
39. Schwirzke F, Taylor R J *J. Nucl. Mater.* **93–94** 780 (1980)
40. Höthker K et al. *J. Nucl. Mater.* **93–94** 785 (1980)
41. Stampa A, Kruger H *J. Phys. D* **16** 2135 (1983)
42. Schwirzke F R *IEEE Trans. Plasma Sci.* **19** 690 (1991)
43. Loarte A et al. *Nucl. Fusion* **47** S203 (2007)
44. Federici G et al. *Nucl. Fusion* **41** 1967 (2001)
45. Roth J et al. *Plasma Phys. Control. Fusion* **50** 103001 (2008)

46. Rohde V et al. *J. Nucl. Mater.* **415** S46 (2011)
47. Rohde V et al. *J. Nucl. Mater.* **438** S800 (2013)
48. Rohde V, Balden M, the ASDEX Upgrade Team *Nucl. Mater. Energy* **9** 36 (2016)
49. Tokitani M et al. *Nucl. Fusion* **51** 102001 (2011)
50. Rudakov D L et al. *J. Nucl. Mater.* **438** S805 (2013)
51. Rudakov D L et al. *Phys. Scr.* **2016** 014055 (2016)
52. Bykov I et al. *Phys. Scr.* **2017** 014034 (2017)
53. Kajita S et al. *Nucl. Fusion* **53** 053013 (2013)
54. Savrukhin P V, Shestakov E A *Phys. Plasmas* **26** 092505 (2019)
55. Dhard C P et al. *Phys. Scr.* **2020** (T171) 014033 (2020)
56. Barengolts S A, Mesyats G A, Tsventukh M M *J. Exp. Theor. Phys.* **107** 1039 (2008); *Zh. Eksp. Teor. Fiz.* **134** 1213 (2008)
57. Federici G, Loarte A, Strohmayer G *Plasma Phys. Control. Fusion* **45** 1523 (2003)
58. Doyle E J et al. *Nucl. Fusion* **47** S18 (2007)
59. Takamura S et al. *Plasma Fusion Res.* **1** 051 (2006)
60. Baldwin M J, Doerner R P *Nucl. Fusion* **48** 035001 (2008)
61. Kajita S et al. *Nucl. Fusion* **49** 095005 (2009)
62. Pitts R A et al. *J. Nucl. Mater.* **438** S48 (2013)
63. De Temmerman G, Hirai T, Pitts R A *Plasma Phys. Control. Fusion* **60** 044018 (2018)
64. Kajita S, Takamura S, Ohno N *Nucl. Fusion* **49** 032002 (2009)
65. Kajita S et al. *Phys. Lett. A* **373** 4273 (2009)
66. Kajita S et al. *Plasma Phys. Control. Fusion* **54** 035009 (2012)
67. Hwangbo D et al. *IEEE Trans. Plasma Sci.* **47** 3617 (2019)
68. Hwangbo D et al. *Contrib. Plasma Phys.* **58** 608 (2018)
69. Hwangbo D et al. *Nucl. Mater. Energy* **12** 386 (2017)
70. Hwangbo D et al. *Results Phys.* **4** 33 (2014)
71. Kajita S et al. *J. Appl. Phys.* **116** 233302 (2014)
72. Barengolts S A et al. *IEEE Trans. Plasma Sci.* **46** 4044 (2018)
73. Aussems D U B et al. *J. Appl. Phys.* **116** 063301 (2014)
74. Hwangbo D et al. *Jpn. J. Appl. Phys.* **52** 11NC02 (2013)
75. Hwangbo D et al. *Plasma Sources Sci. Technol.* **29** 125015 (2020)
76. Barengolts S A et al. *Nucl. Fusion* **60** 044001 (2020)
77. Hwangbo D et al. *IEEE Trans. Plasma Sci.* **45** 2080 (2017)
78. Barengolts S A, Mesyats G A, Tsventoukh M M *IEEE Trans. Plasma Sci.* **39** 1900 (2011)
79. Nishijima D et al. *J. Nucl. Mater.* **415** S96 (2011)
80. Kajita S et al. *Results Phys.* **6** 877 (2016)
81. Barengolts S A, Mesyats G A, Tsventoukh M M *Nucl. Fusion* **50** 125004 (2010)
82. Zinov'ev V E *Teplofizicheskie Svoistva Metallov pri Vysokikh Temperaturakh* (Thermophysical Properties of Metals at High Temperatures) (Moscow: Metallurgiya, 1989) Handbook
83. Kimblin C W *J. Appl. Phys.* **44** 3074 (1973)
84. Anders A et al. *IEEE Trans. Plasma Sci.* **33** 1532 (2005)
85. Zeldovich Y B, Rayzer Y P *Physics of Shock Waves and High-Temperature Hydrodynamic Phenomena* (New York: Academic Press, 1966, 1967); Translated from Russian: *Fizika Udarnykh Voln i Vysokotemperaturnykh Gidrodinamicheskikh Yavlenii* (Moscow: Nauka, 1966)
86. Anders A *Phys. Rev. E* **55** 969 (1997)
87. Anders A et al. *Plasma Sources Sci. Technol.* **12** 63 (1992)
88. Onufriev S V *High Temp.* **49** 205 (2011); *Teplofiz. Vys. Temp.* **49** 213 (2011)
89. Smirnov R D et al. *Phys. Plasmas* **22** 012506 (2015)
90. De Temmerman G, Doerner R P, Pitts R A *Nucl. Mater. Energy* **19** 255 (2019)
91. Agee F J *IEEE Trans. Plasma Sci.* **26** 235 (1998)
92. Guignard G (Ed.), CERN 2000-008 (Geneva: CERN, 2000)
93. Aicheler M et al. (Eds), CLIC Conceptual Design Report CERN 2012-007 (Geneva: CERN, 2012)
94. Wuensch W, CERN-OPEN-2014-028, CLIC-Note-1025 (Geneva: CERN, 2013)
95. Wu X et al. *Phys. Rev. Accel. Beams* **20** 052001 (2017)
96. Wuensch W et al. *Phys. Rev. Accel. Beams* **20** 011007 (2017)
97. Degiovanni A, Wuensch W, Giner Navarro J *Phys. Rev. Accel. Beams* **19** 032001 (2016)
98. Grudiev A, Calatroni S, Wuensch W *Phys. Rev. ST Accel. Beams* **12** 102001 (2009)
99. Descoeudres A et al. *Phys. Rev. ST Accel. Beams* **12** 092001 (2009)
100. Barbour J P et al. *Phys. Rev.* **92** 45 (1953)
101. Barengolts S A, Kreindel M Y, Litvinov E A *IEEE Trans. Plasma Sci.* **26** 252 (1998)
102. Sokolovski D, Baskin L M *Phys. Rev. A* **36** 4604 (1987)
103. Wang J W, Loew G A, in *Frontiers of Accelerator Technology. Proc. of the Joint US-CERN-Japan Intern. School, Hayama/Tsukuba, Japan, 9–18 September 1996* (Eds S I Kurokawa, M Month, S Turner) (Singapore: World Scientific, 1999) p. 768, https://doi.org/10.1142/9789814447324_0024
104. Barengolts S A, Uimanov I V, Shmelev D L *IEEE Trans. Plasma Sci.* **47** 3400 (2019)
105. Uimanov I V, Shmelev D L, Barengolts S A *J. Phys. D* **54** 065205 (2020)
106. Miller S̊ (Jr.), Good R H (Jr.) *Phys. Rev.* **91** 174 (1953)
107. Murphy E L, Good R H (Jr.) *Phys. Rev.* **102** 1464 (1956)
108. Anisimov S I, Imas Ya A, Romanov G S, Khodyko Yu V *Deistvie Izlucheniya Bol'shoi Moshchnosti na Metally* (Effect of High Power Radiation on Metals) (Eds A M Bonch-Bruevich, M A El'yashevich) (Moscow: Nauka, 1970)
109. Nordlund K, Djurabekova F *Phys. Rev. ST Accel. Beams* **15** 071002 (2012)
110. Pritzkau D P, Siemann R H *Phys. Rev. ST Accel. Beams* **5** 112002 (2002)
111. Simakov E I, Dolgashev V A, Tantawi S G *Nucl. Instrum. Meth. Phys. Res. A* **907** 221 (2018)
112. Barengolts S A et al. *IEEE Trans. Plasma Sci.* **49** 2470 (2021)